Received: 5 April 2023 | Revised: 8 August 2023 | Accepted: 16 August 2023

DOI: 10.1002/mma.9651

RESEARCH ARTICLE

WILEY

Investigations of effective dispersion models for electroosmotic flow with rigid and free boundaries in a thin strip

Raphael Schulz[1] | **Stephan Gärttner**[2] | **Nadja Ray**[1,2]

[1]Mathematical Institute for Machine Learning and Data Science, Catholic University of Eichstätt-Ingolstadt, Ingolstadt, Germany

[2]Modelling and Numerics, Department of Mathematics, University of Erlangen–Nürnberg, Erlangen, Germany

Correspondence
Raphael Schulz, Mathematical Institute for Machine Learning and Data Science, Catholic University of Eichstätt-Ingolstadt, Goldknopfgasse 7, 85049 Ingolstadt, Germany.
Email: Raphael.Schulz@ku.de

Communicated by: D. Zeidan

Funding information
DFG Research Training Group 2339; DFG Research Unit 2179

Reactive flow and transport in porous media is topic of intense research since decades. Since dispersion is one of the key parameters in solute transport, its accurate modeling is essential to avoid wrong predictions of flow and transport behavior. In this research, we investigate novel effective dispersion models for reactive transport of electrically charged chemical species in a thin, potentially evolving strip taking into account Taylor–Aris and electroosmotic-induced dispersion as well as their cross-coupling effects. We prove positivity of the dispersion coefficient and the existence and uniqueness of strong solutions in the fixed geometry setting. Moreover, we numerically investigate scenarios for both the fixed and evolving geometry situation. The simulation results illustrate the possibility of separating charged species, such that the findings of this study can lead to a better understanding of mixing and separation processes of charged solutes and an improved prediction of breakthrough curves. Finally, we study the limits of vanishing channel width, precipitation layer thickness, and molecular diffusion. We show convergence of the solutions to the corresponding limit cases such as a hyperbolic model or the fixed geometry case. From these results, we can rate the impact of distinct dispersion mechanisms and evaluate the necessity of a detailed modeling for different parameter regimes.

KEYWORDS

electrodispersion, electroosmosis, evolving microstructure, existence, numerical simulations, Taylor dispersion

MSC CLASSIFICATION

76S05, 74A65, 74Q15, 80A32, 35-XX, 35Q92

1 | INTRODUCTION

Electrokinetic phenomena have a wide range of applications in nanofluidics and microfluidics and in porous media such as desalination and remediation [1–4]. In this context, dispersion is a key parameter. Going beyond classical Taylor dispersion [5, 6], its combination with electroosmotically induced dispersion is essential. In microfluidic devices or

applications including narrow channels, electroosmotic flow becomes attractive, while pressure-driven flow is impractical since pumping requirements become prohibitive; see Jacob and Masliyah [2, Chapter 8]. Electroosmotic flow additionally has the advantage that uniform (plug-like) flow fields leading to less dispersion may be created. The interplay and relative strength of pressure-driven and electroosmotically induced dispersion is therefore crucial for applications such as fractionation, separation, or mixing of chemical species. Although the importance of such dispersion phenomena for practical applications is well-known, detailed numerical and analytical investigations are scarce. Since sophisticated models may easily become computationally demanding, in particular, if evolving geometries are present, often simple geometries such as thin strips and/or effective/upscaled models are considered.

In the fixed geometry case, effective models including Taylor dispersion were derived by formal upscaling techniques in earlier studies [7, 8] stating its quadratic dependence on the velocity field. Reactive flow under dominating convective transport and reaction was (rigorously) studied, and analytical solutions of the corresponding models were investigated in a series of papers by Mikelic and coworkers [9–14]. In more detail, in previous research [11, 12], the rigorously derived effective models were justified by means of error estimates, which gave the approximation error as a power of the scaling parameter. The applied technique of anisotropic singular perturbations was continued to the situation of reactive transport with adsorption–desorption through a strip in van Duijn et al. [14], while alterations of the underlying microstructure were disregarded.

However, the underlying pore geometry may significantly alter due to several processes which possibly have a high impact on the performance or applicability of technical devices. Since experimental settings are often accompanied with (unwanted) pore changing processes, these effects need to be incorporated in accurate, predictive modeling. Model extensions taking into account such alterations in the transport dominated realm were studied in earlier research [15, 16]. In the situation of a thin strip, the quadratic dependence of Taylor dispersion on the velocity field was derived by asymptotic analysis.

In Schmuck and Bazant [17], the results from Allaire et al. [9] were extended to electrohydrodynamics while focusing on pressure-driven flow and neglecting electroosmotic flow. Effective models including electroosmotically induced dispersion are well-known in the engineering literature [2]. In earlier studies [18, 19], Taylor dispersion due to combined pressure-driven and electroosmotically induced flows within a thin porous channel was investigated via asymptotic analysis. In order to describe electro-osmotic flow and neutral solute transport, effective dispersion coefficients were derived for soft microchannels in Hoshyargar et al. [20], for channels with dense polyelectrolyte layer in Talebi et al. [21], for channels containing elastic macromolecules in Hoshyargar et al. [22], and for fouling processes in Ayoubi et al. [23].

In Ray and Schulz [24], the results obtained in previous studies [2, 16, 25] were consistently extended, that is, upscaling reactive flow and transport in a thin channel, while taking into account dominant pressure-driven and electroosmotic flow as well as a potentially evolving microstructure due to precipitation/dissolution reactions. In detail, two situations were considered: First, the crystal precipitant formed a very thin layer and was explicitly modeled by the concentration of the immobile product. Second, the thickness of the deposited layer was assumed to be not negligible. As a result of the upscaling procedure, a one-dimensional (fully) coupled ODE-PDE model was obtained, for which explicit relations for electroosmotically induced dispersion were derived and its cross-coupling with dispersion stemming from pressure-driven flow was revealed. As in the regime of pure Taylor dispersion, all terms inherit a (weighted) dependence on the respective velocities squared.

The subject of this research is to build upon these effective models [24] and to address them from both analytical and numerical perspectives. First, we prove local-in-time existence of strong solutions in the situation of a fixed geometry setting using a fixed point approach. Although the effective model is just one-dimensional and only partially coupled, it has specific challenges. On the one hand, quite demanding dispersion coefficients are present, which contain various components (pressure-driven Taylor-dispersion, electroosmotic-induced dispersion, and cross-coupling terms). Thereby, applying methods from complex analysis, we show positivity of these coefficients, which is crucial for analytical results. On the other hand, the coupling of the ODE-PDE model is nonlinear. In addition to numerous technical terms, the derivative of the reaction rate enters the right side; see Section 2, which is nonstandard and not easy to control. In case of an evolving geometry, the situation is more involved. Then the weights are modulated by the opening width of the thin strip, and the flow field does not have a constant profile such that transport, geometry, and flow are fully coupled. This makes numerical studies more sophisticated than in the situation of fixed geometry setting due to the increasing stiffness of the overall problem. Respecting this fact, we refrain from applying iterative solution schemes but treat the system of differential-algebraic equation obtained after discretization in a monolithical manner with adaptive time-stepping.

In terms of numerics, similar settings were investigated in the context of crystal precipitation and dissolution in earlier studies [25, 26], biofilm growth in van Noorden et al. [27], transport under general interaction potentials in other research

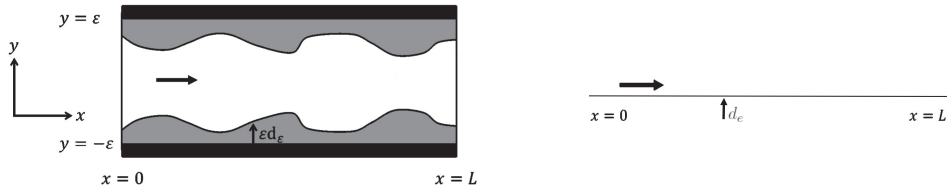

FIGURE 1 Left: pore scale setting for an evolving geometry. Right: corresponding effective model.

[28, 29], and reactive flows under dominant convection in previous literature [15, 16]. Consistency with simplified models was shown by investigating certain limit regimes in other studies [15, 16]. Moreover, the obtained models for fixed and evolving geometry were compared.

Likewise, we investigate the limit $\rho \to \infty$ which corresponds to the situation of a thin but highly dense precipitation layer, and therefore, the limit corresponds to the fixed geometry situation. Moreover, we show convergence of our model to a hyperbolic limit model ($\varepsilon = 0$) by numerically investigating the limit $\varepsilon \to 0$. Finally, we investigate the limit $D \to 0$, which allows us to weight the contributions of the distinct dispersive terms. The steepness of the concentration profiles and the precipitation's distribution is influenced by these dispersive terms. These results enable us to rate the impact of distinct dispersion mechanisms and evaluate the necessity of a detailed modeling for different parameter regimes. Moreover, the results that illustrate the possibility of separating charged species, which open up ways for improved predictions of breakthrough curves as well as facilitated modeling of mixing and separation processes, are possible. In this sense, the current work contributes to the improvement and extension of the fundamental understanding of flow and transport processes.

The paper is organized as follows: In Section 2, we recall the model equations for dispersive transport in an potentially evolving thin channel, which were derived in Ray and Schulz [24]. We consider the positivity of the corresponding dispersion coefficient. Then the model for the fixed geometry is analyzed for existence of strong solutions thereafter in Section 3. These investigations are complemented with numerical simulations in Section 4. Finally, in Section 5, we conclude the paper with a brief discussion of the obtained results and outline directions of further research.

2 | MODELS

At the pore scale, we consider [24] a charged, narrow channel, geometrically represented by a thin strip $(0, L) \times (-\varepsilon, \varepsilon)$ with small height $\varepsilon > 0$ as depicted in Figure 1, left. Such a thin strip represents, for instance, a single pore, a fracture, or a microfluidic device. Hereby, the thickness of the boundary layer due to precipitated chemical species is $\varepsilon d_\varepsilon$.

In this research, we consider the corresponding effective models derived from asymptotic analysis in Ray and Schulz [24] by averaging quantities of interest with respect to the small height; see Figure 1, right. We emphasize at this point the principle limitations of effective models, which are still valuable despite their simplicity. Although the model's applicability is restricted in terms of the underlying geometry, that is, for a very small scaling parameter $\varepsilon > 0$, it provides useful insights into the present flow and transport problems considered. Moreover, in the specific situation of an evolving thin strip, the model is constrained by the assumption that the boundary layer's thickness can be represented as the graph of a function according to x.

A fluid, in which dissolved electrically charged chemical species with concentrations $\bar{c}_e^{\pm}$ are present, flows through a one-dimensional domain $\Omega = (0, L)$ with $L > 0$. The species' and induced channel's charges (zeta potential) give rise to electroosmotic flow $\bar{v}_{e,EO}$ in addition to pressure-driven flow $\bar{v}_{e,P}$. The chemical species $\bar{c}_e^+$ and $\bar{c}_e^-$ (abbreviated as $\bar{c}_e^{\pm}$ in the following) are transported by convection (related to pressure-driven and electroosmotic flow), electric drift (related to electrophoretic flow induced by electric potential difference $\Phi_r - \Phi_l$), diffusion, and Taylor/electroosmotic-induced dispersion. They additionally undergo chemical reactions of the type $c^+ + c^- \leftrightarrow c^{im}$ with the immobile product c_e^{im}. Under the assumption of mass action kinetics (disregarding the reaction rate coefficients), this leads to $f\left(\bar{c}_e^+, \bar{c}_e^-, c_e^{im}\right) = \bar{c}_e^+ \bar{c}_e^- - c_e^{im}$. As parameters, the zeta potential ζ and the Debye length κ, enter the model as dimensionless characteristic positive number. The diffusion coefficient D as well as the functions $F^{(0)}, F^{(1)}, F^{(2)}$ highlight the contributions of the distinct dispersive terms.

Two different situations are considered in this paper: First, in Model 1, we explicitly consider the concentration of the immobile product. This reflects situations, in which the crystal precipitant forms a very thin layer, for example, due to its high density ρ.

Model 1 (External electric field and double layer potential, fixed geometry)**.**

Transport equation for mobile species

$$\begin{aligned}
&\partial_t\left(\bar{c}_e^{\pm}+c_e^{im}\right)+\partial_x\left(\bar{v}_e^{(1)}\bar{c}_e^{\pm}\right)\\
&-\varepsilon\partial_x\left(D\left(1+\frac{1}{D^2}\left[\frac{2}{105}\left(\bar{v}_{e,P}^{(1)}\right)^2-\frac{2F^{(1)}(\kappa)}{15\kappa}\bar{v}_{e,P}^{(1)}\bar{v}_{e,EO}^{(1)}+\frac{F^{(0)}(\kappa)}{12\kappa^2}\left(\bar{v}_{e,EO}^{(1)}\right)^2\right]\right)\partial_x\bar{c}_e^{\pm}\right)\\
&+\varepsilon\partial_x\left(\left[\frac{1}{15D}\bar{v}_{e,P}^{(1)}-\frac{F^{(2)}(\kappa)}{3D\kappa}\bar{v}_{e,EO}^{(1)}\right]f\left(\bar{c}_e^{+},\bar{c}_e^{-},c_e^{im}\right)\right)\pm\varepsilon\partial_x\left(E\bar{c}_e^{\pm}\right)=0 \qquad \text{in } [0,L],
\end{aligned}$$

where the κ-depending functions $F^{(i)}$, $i=0,1,2$, are defined as follows:

$$\begin{aligned}
F^{(0)}(\kappa)&=\frac{4(6+\kappa^2)\sinh^2(\kappa)-9\kappa\sinh(2\kappa)-6\kappa^2}{(\kappa\cosh(\kappa)-\sinh(\kappa))^2},\\
F^{(1)}(\kappa)&=\frac{(-\kappa^4+15\kappa^2+45)\sinh(\kappa)-45\kappa\cosh(\kappa)}{\kappa^3(\kappa\cosh(\kappa)-\sinh(\kappa))} \quad\text{and}\quad F^{(2)}(\kappa)=\frac{(-\kappa^2-3)\sinh(\kappa)+3\kappa\cosh(\kappa)}{\kappa(\kappa\cosh(\kappa)-\sinh(\kappa))}.
\end{aligned}$$

Evolution equation for immobile species

$$\begin{aligned}
&\left(1+\varepsilon\frac{1}{3}\frac{\partial_1 f\left(\bar{c}_e^{+},\bar{c}_e^{-},c_e^{im}\right)+\partial_2 f\left(\bar{c}_e^{+},\bar{c}_e^{-},c_e^{im}\right)}{D}\right)\partial_t c_e^{im}=f\left(\bar{c}_e^{\pm},c_e^{im}\right)\\
&+\varepsilon\left(\frac{1}{15}\frac{\bar{v}_{e,P}^{(1)}}{D}+\frac{E\zeta}{D}\left(\frac{1}{\kappa^2}-\frac{1}{\kappa^4}-\frac{1}{3}\frac{\tanh(\kappa)}{\kappa}\right)\right)\left(\partial_1 f\left(\bar{c}_e^{+},\bar{c}_e^{-},c_e^{im}\right)\partial_x\bar{c}_e^{+}+\partial_2 f\left(\bar{c}_e^{+},\bar{c}_e^{-},c_e^{im}\right)\partial_x\bar{c}_e^{-}\right) \qquad \text{in } [0,L].
\end{aligned}$$

Darcy's law and electroosmotic flow and pressure

$$\begin{aligned}
\bar{v}_e^{(1)}&=-\frac{1}{3}\partial_x p_e-E\zeta\left(1-\frac{\tanh(\kappa)}{\kappa}\right)=:\bar{v}_{e,P}^{(1)}+\bar{v}_{e,EO}^{(1)} \qquad \text{in } [0,L],\\
\partial_x\bar{v}_e^{(1)}&=0 \qquad \text{in } [0,L].
\end{aligned}$$

Electric field

$$-E=\frac{\phi_r-\phi_l}{L} \qquad \text{in } [0,L].$$

Secondly, in Model 2, we assume that the thickness d_e of the deposited layer with density ρ is not negligible, as occurs, for example, at high species concentrations. In this situation, the thickness of the layer d_e substitutes the immobile concentration as an additional unknown.

Model 2 (External electric field and double layer potential, evolving geometry)**.**

Transport equation for mobile species

$$\begin{aligned}
&\partial_t\left((1-d_e)\bar{c}_e^{\pm}+\rho d_e\right)+\partial_x\left((1-d_e)\bar{v}_e^{(1)}\bar{c}_e^{\pm}\right)\\
&-\varepsilon\partial_x\left((1-d_e)D\left(1+\frac{1}{D^2}\left[\frac{2}{105}\left((1-d_e)\bar{v}_{e,P}^{(1)}\right)^2-\frac{2F^{(1)}((1-d_e)\kappa)}{15\kappa}\bar{v}_{e,P}^{(1)}\bar{v}_{e,EO}^{(1)}\right.\right.\right.\\
&\left.\left.\left.+\frac{F^{(0)}((1-d_e)\kappa)}{12\kappa^2(1-d_e)^2}\left(\bar{v}_{e,EO}^{(1)}\right)^2\right]\right)\partial_x\bar{c}_e^{\pm}\right)\\
&+\varepsilon\partial_x\left(\left[\frac{(1-d_e)^2}{15D}\bar{v}_{e,P}^{(1)}-\frac{F^{(2)}((1-d_e)\kappa)}{3D\kappa}\bar{v}_{e,EO}^{(1)}\right]f(\bar{c}_e^{+},\bar{c}_e^{-},\rho d_e)\right)\pm\varepsilon E\partial_x\bar{c}_e^{\pm}=0 \text{ in } [0,L].
\end{aligned}$$

	Fixed microstructure	Evolving microstructure
Molecular diffusion	D	$\bar{d}_e D$
Taylor dispersion	$D\left(\frac{1}{D^2}\frac{2}{105}\bar{v}_{e,P}^2\right)$	$\bar{d}_e D\left(1+\frac{1}{D^2}\frac{2}{105}(\bar{d}_e\bar{v}_{e,P})^2\right)$
Electroosmotic dispersion	$D\left(\frac{1}{D^2}\frac{F^{(0)}(\kappa)}{12\kappa^2}\bar{v}_{e,EO}^2\right)$	$\bar{d}_e D\left(\frac{1}{D^2}\frac{F^{(0)}(a)}{12a^2}\bar{v}_{e,EO}^2\right)$
Cross-coupling term	$-\frac{1}{D}\frac{2F^{(1)}(\kappa)}{15\kappa}\bar{v}_{e,P}\bar{v}_{e,EO}$	$-\frac{\bar{d}_e}{D}\frac{2F^{(1)}(a)}{15\kappa}\bar{v}_{e,P}\bar{v}_{e,EO}$
Entire dispersive term for small κ	$D\left(1+\frac{1}{D^2}\frac{2}{105}\left[\bar{v}_{e,P}+\bar{v}_{e,EO}\right]^2\right)$	$\bar{d}_e D\left(\frac{\bar{d}_e^2}{D^2}\frac{2}{105}\left[\bar{v}_{e,P}+\frac{a^2}{3d_e}\bar{v}_{e,EO}\right]^2\right)$

TABLE 1 Overview of different regimes and summary of the corresponding effective dispersion terms, where we introduced $\bar{d}_e = 1 - d_e$ and $a = \kappa\bar{d}_e$.

Evolution equation for the moving boundary

$$\begin{aligned}&\left(1+\varepsilon\frac{1}{3}\frac{\partial_1 f(\bar{c}_e^+,\bar{c}_e^-,\rho d_e)+\partial_2 f(\bar{c}_e^+,\bar{c}_e^-,\rho d_e)}{D}\rho(1-d_e)\right)\partial_t d_e\\ &= f(\bar{c}_e^{\pm},\rho d_e)+\varepsilon\left(\frac{1}{15}\frac{\bar{v}_e^{(1)}}{D}(1-d_e)^2+\frac{E\zeta}{D}\left(\frac{1}{\kappa^2(1-d_e)}-\frac{1}{\kappa^4(1-d_e)^2}-\frac{1}{3}\frac{\tanh(\kappa(1-d_e))}{\kappa}\right)\right)\\ &\quad\cdot\left(\partial_1 f(\bar{c}_e^+,\bar{c}_e^-,\rho d_e)\partial_x\bar{c}_e^+ + \partial_2 f(\bar{c}_e^+,\bar{c}_e^-,\rho d_e)\partial_x\bar{c}_e^-\right)\\ &\qquad\qquad\text{in } [0,L].\end{aligned}$$

Darcy's law and electroosmotic flow and pressure

$$\begin{aligned}\bar{v}_e^{(1)} = -\frac{1}{3}(1-d_e)^2\partial_x p_e - \frac{E\zeta}{1-d_e}\left(1-\frac{\tanh(\kappa(1-d_e))}{\kappa(1-d_e)}\right) =: \bar{v}_{e,P}^{(1)}+\bar{v}_{e,EO}^{(1)} \quad \text{in } [0,L],\\ \partial_x\left((1-d_e)\bar{v}_e^{(1)}\right) = \partial_t d_e \quad \text{in } [0,L].\end{aligned}$$

Electric field

$$-E = \langle 1-d_e\rangle\frac{\phi_r-\phi_l}{L} \qquad \text{in } [0,L].$$

Additionally, suitable initial conditions and boundary conditions on the inflow and outflow boundary supplement the model equations. These are outlined below in Theorem 1 for the analysis and in Table 2 for numerics, respectively.

In the following Table 1, the dispersion coefficients for the situations with fixed/evolving geometry as well as its contributions from pressure and electroosmotic origin are listed. Additionally, the limit of small Debye length κ is outlined following the investigations in Ray and Schulz [24]. The relation between the distinct models as well as the analytical and numerical investigations conducted in Sections 3 and 4 is outlined in the following remarks and illustrated in Figure 2.

Remark 1. Models 1 and 2 can be simplified by disregarding the double layer effect and just taking into account the external electric field. The reduced model is obtained by setting $\zeta = 0$, which additionally results in $v_{e,EO} = 0$. This model is later on additionally used for numerical investigations in Section 4. If also the external electric field E is disregarded, the usual Taylor dispersion model is obtained in either of the two situations, fixed geometry or evolving geometry.

Remark 2. Later on in Section 4, for the sake of comparison to further upscaled models, the hyperbolic limit model is additionally considered. This reduced model is obtained by setting $\varepsilon = 0$ in Models 1 and 2.

Remark 3. Scaling the velocity $\bar{v}_e^{(1)}$ by $1-d_e$ leads to the well-known Darcy's law expressed in terms of the Darcy velocity. We emphasize the different scaling properties of the pressure-driven and electroosmotic-driven velocity contributions.

$$\begin{aligned}\bar{q}_{e,total}^{(1)} = -\frac{1}{3}(1-d_e)^3\partial_x p_e - E\zeta\left(1-\frac{\tanh(\kappa(1-d_e))}{\kappa(1-d_e)}\right) =: \bar{q}_e^{(1)}+\bar{q}_{e,EO}^{(1)} \quad \text{in } [0,L],\\ \partial_x\left(\bar{q}_{e,total}^{(1)}\right) = \partial_t d_e \quad \text{in } [0,L].\end{aligned} \tag{1}$$

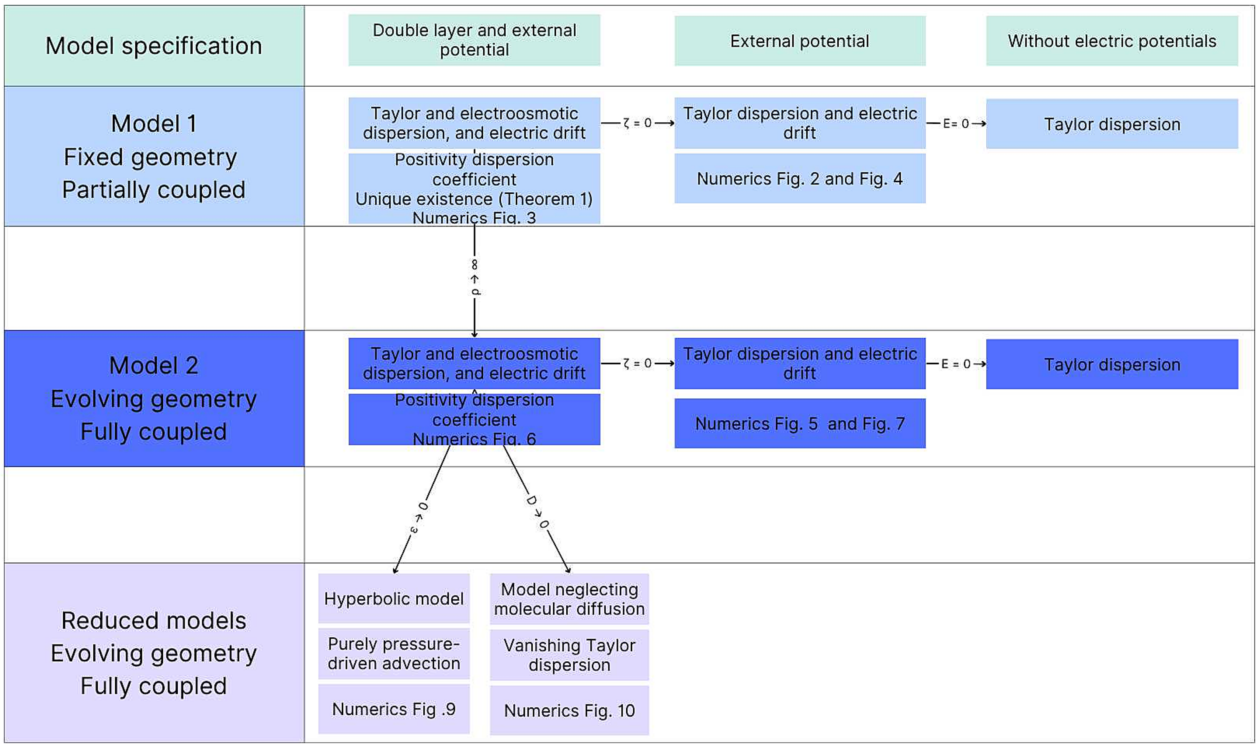

FIGURE 2 Overview of different models and investigations. [Colour figure can be viewed at wileyonlinelibrary.com]

This underpins the applicability of electroosmotic driven flow in thin channels since the contribution does not scale with the channel opening.

3 | ANALYSIS

In this section, we deal with the mathematical analysis of Model 1 corresponding to the fixed geometry setting. First, we investigate in Section 3.1 the dispersion coefficient, since positivity is crucial for the models analysis in the framework of standard parabolic existence theory [30]. Then we prove the main result; see Theorem 1 below, in Section 3.2.

In the following, the norm of the Lebesgue space L^p, $p \in [1,\infty]$, is denoted by $\|.\|_p$. For norms of time-and space-dependent functions c, the standard notation is used, for example, $\|c\|_{L^2(L^\infty)} = \left(\int_0^T \|c(t)\|_\infty^2 dt\right)^{\frac{1}{2}}$ for $c \in L^2(0,T;L^\infty(\Omega))$. We introduce an appropriate function space for strong solutions:

$$X = \left\{c \in L^2(0,T;H^2(\Omega)) \cap L^\infty(0,T;H_0^1(\Omega)) \ : \ \partial_t c \in L^2(0,T;L^2(\Omega))\right\},$$

where this space equipped with the norm

$$\|c\|_X := \sup_{t\in(0,T)} \|c(t)\|_{H^1} + \|c\|_{L^2(0,T;H^2(\Omega)} + \|\partial_t c\|_{L^2(0,T;L^2(\Omega))} \tag{2}$$

is a Banach space.

Theorem 1 (Strong solvability of Model 1)**.** *Let the parameters and the reaction rate be given as described in Section 2. We consider Model 1 equipped with homogeneous Dirichlet boundary conditions for the mobile species $\bar{c}_e^\pm$ and pressure boundary data $p(0) = p_l, p(L) = p_r$. Moreover, let $c_{e,0}^\pm \in H_0^1(\Omega)$ and $c_{e,0}^{im} \in H^1(\Omega)$ be the initial data of mobile and immobile species, respectively. Then for sufficiently small $T > 0$, there exists a unique pair of strong solutions*

$$\begin{aligned} &\bar{c}_e^\pm \in X \qquad \text{and} \\ &c_e^{im} \in \left\{c \in L^\infty(0,T;H^1(\Omega)) \ : \ \partial_t c \in L^2(0,T;L^2(\Omega))\right\}. \end{aligned} \tag{3}$$

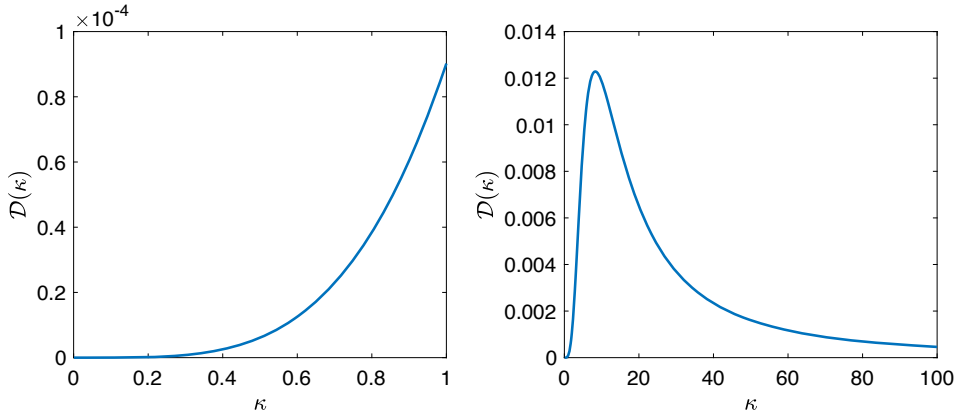

FIGURE 3 Plots of $\mathcal{D}(\kappa)$ in different ranges around zero. [Colour figure can be viewed at wileyonlinelibrary.com]

3.1 | Positivity of the dispersion coefficient

To prove the positivity of the dispersion coefficient, we reformulate the corresponding expression given in Model 1 as follows:

$$\begin{aligned}\mathbb{D} &= D\left(1+\frac{1}{D^2}\left[\frac{2}{105}\left(\bar{v}_{e,P}^{(1)}\right)^2-\frac{2F^{(1)}(\kappa)}{15\kappa}\bar{v}_{e,P}^{(1)}\bar{v}_{e,EO}^{(1)}+\frac{F^{(0)}(\kappa)}{12\kappa^2}\left(\bar{v}_{e,EO}^{(1)}\right)^2\right]\right)\\ &= D\left(1+\frac{1}{D^2}\frac{2}{105}\left\{\left[\bar{v}_{e,P}^{(1)}-\frac{7F^{(1)}(\kappa)}{2\kappa}\bar{v}_{e,EO}^{(1)}\right]^2+\mathcal{D}(\kappa)\left(\bar{v}_{e,EO}^{(1)}\right)^2\right\}\right),\end{aligned} \tag{4}$$

where $\mathcal{D}(\kappa)=\frac{7}{4\kappa^2}\left[\frac{5}{2}F^{(0)}(\kappa)-7(F^{(1)}(\kappa))^2\right]$. The strict positivity of the dispersion coefficient, that is, $\mathbb{D}>0$, is ensured since the function $\mathcal{D}(\kappa)$ is nonnegative for all $\kappa\in\mathbb{R}$, compare Figure 3.

For sufficiently small κ, the dispersive term can be replaced as outlined in Table 1, such that the positivity is guaranteed. For large $\kappa\geq 10$, on the other hand, this property can be shown as follows: The nonnegativity of $\mathcal{D}(\kappa)$ is equivalent to

$$\begin{aligned}\tilde{\mathcal{D}}(\kappa) &:= \frac{4\kappa^2}{7}\cdot\kappa^6\cdot(\kappa\cosh(\kappa)-\sinh(\kappa))^2\mathcal{D}(\kappa)\\ &= \frac{5}{2}\kappa^6\left[4(6+\kappa^2)\sinh^2(\kappa)-9\kappa\sinh(2\kappa)-6\kappa^2\right]\\ &\quad -7\left[(-\kappa^4+15\kappa^2+45)\sinh(\kappa)-45\kappa\cosh(\kappa)\right]^2\geq 0.\end{aligned} \tag{5}$$

With $\sinh(2\kappa)=2\sinh(\kappa)\cosh(\kappa)$ and $\cosh^2(\kappa)=1+\sinh^2(\kappa)$, we obtain

$$\begin{aligned}\tilde{\mathcal{D}}(\kappa) &= 10\kappa^6(6+\kappa^2)\sinh^2(\kappa)-45\kappa^7\sinh(\kappa)\cosh(\kappa)-15\kappa^8\\ &\quad -7\left[(-\kappa^4+15\kappa^2+45)^2\sinh^2(\kappa)-2(-\kappa^4+15\kappa^2+45)\sinh(\kappa)45\kappa\cosh(\kappa)\right.\\ &\quad \left.+45^2\kappa^2(1+\sinh^2(\kappa))\right]^2\\ &= \left[(10+1)\kappa^8+(60-30)\kappa^6+(15^2-90)\kappa^4+(-7\cdot 45^2+30\cdot 45)\kappa^2+45^2\right]\sinh^2(\kappa)\\ &\quad +\left[-45\kappa^7-14\cdot 45\kappa^5+14\cdot 15\cdot 45\kappa^3+14\cdot 45^2\kappa\right]\sinh(\kappa)\cosh(\kappa)\\ &\quad +\left[-15\kappa^8-7\cdot 45^2\kappa^2\right].\end{aligned} \tag{6}$$

Replacing sinh and cosh by their exponential representations yields

$$\begin{aligned}\tilde{\mathcal{D}}(\kappa) = &\left[11\kappa^8+30\kappa^6+135\kappa^4-12825\kappa^2+2025\right]\frac{1}{4}\left(e^{2\kappa}-2+e^{-2\kappa}\right)\\ &+\left[-45\kappa^7-630\kappa^5+9450\kappa^3+28350\kappa\right]\frac{1}{4}\left(e^{2\kappa}-e^{-2\kappa}\right)\\ &+\left[-15\kappa^8-14175\kappa^2\right]\end{aligned}$$

$$
\begin{aligned}
&= \frac{1}{4}\left[11\kappa^8 - 45\kappa^7 + 30\kappa^6 - 630\kappa^5 + 135\kappa^4 + 9450\kappa^3 - 12825\kappa^2 + 28350\kappa + 2025\right] e^{2\kappa} \\
&\quad + \frac{1}{4}\left[11\kappa^8 + 45\kappa^7 + 30\kappa^6 + 630\kappa^5 + 135\kappa^4 - 9450\kappa^3 - 12825\kappa^2 - 28350\kappa + 2025\right] e^{-2\kappa} \\
&\quad - \left[\left(\frac{11}{2} + 15\right)\kappa^8 + 15\kappa^6 + \frac{135}{2}\kappa^4 + \left(-\frac{12825}{2} + 14175\right)\kappa^2 + \frac{2025}{2}\right] \\
&=: \frac{1}{4}P_1(\kappa)e^{2\kappa} + \frac{1}{4}P_2(\kappa)e^{-2\kappa} - P_3(\kappa).
\end{aligned} \tag{7}
$$

Then Rouché's theorem, see Theorem A.1 in the Appendix, yields $P_1(\kappa) > 0$ and $P_2(\kappa) > 0$ for $\kappa \geq 10$ since

$$
\begin{aligned}
11 \cdot 10^8 > 45 \cdot 10^7 + 30 \cdot 10^6 + 630 \cdot 10^5 + 135 \cdot 10^4 + 9450 \cdot 10^3 \\
+ 12825 \cdot 10^2 + 28350 \cdot 10 + 2025,
\end{aligned} \tag{8}
$$

that is, P_1 and P_2 have all their zeros within the open disk $\{z \in \mathbb{C} : |z| < 10\}$. Due to the positivity of P_2, we can estimate for an appropriate $\ell \in \mathbb{N}$

$$
\tilde{D}(\kappa) > \frac{1}{4}P_1(\kappa)e^{2\kappa} - P_3(\kappa) > \frac{1}{4}P_1(\kappa)\frac{(2\kappa)^\ell}{\ell!} - P_3(\kappa) \overset{!}{\geq} 0. \tag{9}
$$

Similar to the above, Rouché's theorem implies nonnegativity of the polynomial $\frac{1}{4}P_1(\kappa)\frac{(2\kappa)^\ell}{\ell!} - P_3(\kappa)$ for $\kappa \geq 10$ and $\ell = 1$.

Remark 4. In the evolving geometry setting, compare Model 2, the dispersion coefficient additionally depends on the thickness d_e of the precipitated layer:

$$
\begin{aligned}
\mathbb{D}_{d_e} &= (1-d_e)D\left(1 + \frac{1}{D^2}\left[\frac{2}{105}\left((1-d_e)\bar{v}_{e,P}^{(1)}\right)^2 - \frac{2F^{(1)}((1-d_e)\kappa)}{15\kappa}\bar{v}_{e,P}^{(1)}\bar{v}_{e,EO}^{(1)} + \frac{F^{(0)}((1-d_e)\kappa)}{12\kappa^2(1-d_e)^2}\left(\bar{v}_{e,EO}^{(1)}\right)^2\right]\right) \\
&= (1-d_e)D\left(1 + \frac{1}{D^2}\frac{2}{105}\left\{\left[(1-d_e)\bar{v}_{e,P}^{(1)} - \frac{7F^{(1)}((1-d_e)\kappa)}{2(1-d_e)\kappa}\bar{v}_{e,EO}^{(1)}\right]^2 + \mathcal{D}((1-d_e)\kappa)\left(\bar{v}_{e,EO}^{(1)}\right)^2\right\}\right).
\end{aligned} \tag{10}
$$

In comparison with the dispersion coefficient $\mathbb{D}$ in the fixed geometry case, the values D, κ, and $\bar{v}_{e,P}^{(1)}$ are scaled by $1 - d_e$. However, the strict positivity of $\mathbb{D}_{d_e}$ again follows from the nonnegativity of $\mathcal{D}$ as outlined above.

3.2 | Proof of Theorem 1: Strong solvability of model 1

In what follows, we discuss the local-in-time strong solvability of the fixed geometry Model 1. As already described above in Section 2, we use $f(c^+, c^-, c^{im}) = c^+c^- - c^{im}$ as a mass and charge conserving reaction rate. We emphasize that the coupling in this model is one-sided. More precisely, the transport equation as well as the evolution equation depend on the electric field, the pressure, and electroosmotic flow, whereas these values are determined directly. Note that the overall velocity $\bar{v}_e^{(1)}$ as well as the pressure driven and the electroosmotic parts are constant for the assumed pressure boundary data $p(0) = p_l, p(L) = p_r$. Therefore, it is sufficient to consider the equations describing im-/mobile species for given electric field and fluid flow. We linearize these equations by substituting a given value $\tilde{c}_e^\pm \geq 0$ for the corresponding unknowns $\bar{c}_e^\pm$ in the reaction rate of the evolution equation for the immobile species and right-hand side of the transport equation for the mobile species. Moreover, we regularize the denominator in the evolution equation for the immobile species by replacing $\tilde{c}_e^\pm$ by

$$
(\tilde{c}_e^\pm)_+ = \begin{cases} \tilde{c}_e^\pm & \tilde{c}_e^\pm \geq 0 \\ 0 & \text{else.} \end{cases} \tag{11}
$$

Later on, we deduce the nonnegativity of the solutions $c_e^{\pm}$ such that the cutoff is redundant. In summary, this leads to the following ODE-PDE system:

$$\begin{aligned}\partial_t c_e^{im} = &\left(1+\varepsilon\frac{1}{3}\,\frac{\left(\tilde{c}_e^{+}\right)_+ + (\tilde{c}_e^{-})_+}{D}\right)^{-1}\\ &\left(\tilde{c}_e^{+}\tilde{c}_e^{-} - c_e^{im} + \varepsilon\left(\frac{1}{15}\frac{\bar{v}_{e,P}^{(1)}}{D} + \frac{E\zeta}{D}\left(\frac{1}{\kappa^2}-\frac{1}{\kappa^4}-\frac{1}{3}\frac{\tanh(\kappa)}{\kappa}\right)\right)\left(\tilde{c}_e^{-}\partial_x\tilde{c}_e^{+}+\tilde{c}_e^{+}\partial_x\tilde{c}_e^{-}\right)\right) \text{ in } [0,L],\end{aligned} \tag{12}$$

$$\begin{aligned}&\partial_t\bar{c}_e^{+} + \partial_x\left(\bar{v}_e^{(1)}\bar{c}_e^{+}\right) - \varepsilon\partial_x\left(\mathbb{D}\partial_x\bar{c}_e^{+}\right) + \varepsilon\partial_x\left(E\bar{c}_e^{+}\right)\\ &= -\partial_t c_e^{im} - \varepsilon\partial_x\left(\left[\frac{1}{15D}\bar{v}_{e,P}^{(1)} - \frac{F^{(2)}(\kappa)}{3D\kappa}\bar{v}_{e,EO}^{(1)}\right]\left(\tilde{c}^{+}\tilde{c}^{-}-c^{im}\right)\right) \quad \text{in } [0,L],\end{aligned} \tag{13a}$$

and

$$\begin{aligned}&\partial_t\bar{c}_e^{-} + \partial_x\left(\bar{v}_e^{(1)}\bar{c}_e^{-}\right) - \varepsilon\partial_x\left(\mathbb{D}\partial_x\bar{c}_e^{-}\right) - \varepsilon\partial_x\left(E\bar{c}_e^{-}\right)\\ &= -\partial_t c_e^{im} - \varepsilon\partial_x\left(\left[\frac{1}{15D}\bar{v}_{e,P}^{(1)} - \frac{F^{(2)}(\kappa)}{3D\kappa}\bar{v}_{e,EO}^{(1)}\right]\left(\tilde{c}^{+}\tilde{c}^{-}-c^{im}\right)\right) \quad \text{in } [0,L].\end{aligned} \tag{13b}$$

For the sake of readability, we introduce the following notations

$$\begin{aligned}A\left(\tilde{c}_e^{\pm}\right) &:= 1+\varepsilon\frac{1}{3}\frac{\left(\tilde{c}_e^{+}\right)_+ + \left(\tilde{c}_e^{-}\right)_+}{D},\\ B &:= \frac{1}{15}\frac{\bar{v}_{e,P}^{(1)}}{D} + \frac{E\zeta}{D}\left(\frac{1}{\kappa^2}-\frac{1}{\kappa^4}-\frac{1}{3}\frac{\tanh(\kappa)}{\kappa}\right),\\ C &:= \frac{1}{15D}\bar{v}_{e,P}^{(1)} - \frac{F^{(2)}(\kappa)}{3D\kappa}\bar{v}_{e,EO}^{(1)},\end{aligned} \tag{14}$$

where B and C are constant with respect to the time and space variable in the fixed geometry setting. Furthermore, we use the intuitive notation

$$\begin{aligned}rhs^{im} &:= A^{-1}\left(\tilde{c}_e^{\pm}\right)\left(\tilde{c}_e^{+}\tilde{c}_e^{-} - c_e^{im} + \varepsilon B\left(\tilde{c}_e^{-}\partial_x\tilde{c}_e^{+}+\tilde{c}_e^{+}\partial_x\tilde{c}_e^{-}\right)\right)\\ rhs^{\pm} &:= -\partial_t c_e^{im} - \varepsilon\partial_x\left(C\left(\tilde{c}^{+}\tilde{c}^{-}-c^{im}\right)\right)\end{aligned} \tag{15}$$

for the right-hand side of (12) or (13), respectively.

Throughout this section, $C>0$ describes positive constants, where the value may differ from one occasion to another.

Applying Banach's fixed-point theorem, compare Theorem A.3 in the Appendix, we prove the existence of a unique strong solution to the original Model 1. In what follows, we describe the crucial steps of the fixed-point argument in more detail:

Step 1: (**Fixed point framework**) We consider the fixed point operator

$$\mathcal{A} : X_0 \to X_0 \tag{16}$$

with respect to the closed subspace

$$X_0 = \left\{ c\in X \,:\, \|c\|_X \le 2M\|c_{e,0}^{\pm}\|_{H^1}\right\} \tag{17}$$

of the underlying function space X. Here $M>0$ is an appropriately chosen constant; see Step 3 below. The operator $\mathcal{A}$ is defined as follows: Let $\tilde{c}_e^{\pm}\in X_0$. We obtain a solution c_e^{im} of (12) and hence by inserting $\tilde{c}_e^{\pm}$ and c_e^{im} on the right-hand side, a solution $c_e^{\pm}$ for Equation 13; see Steps 2 and 3. Finally, the operator $\mathcal{A}$ is defined by $\mathcal{A}\left(\tilde{c}_e^{\pm}\right) = c_e^{\pm}$.

Step 2: (**Analyzing the ordinary differential equation (ODE)** (12)) Let us start considering the modified evolution equation of the immobile species. The right-hand side of (12) is Lipschitz continuous with respect to c_e^{im}. Assuming $\tilde{c}_e^{\pm} \in X$, it is guaranteed by standard results (e.g., Evans [30, Theorem 3, Chapter 5.9]) that $\tilde{c}_e^{\pm} \in C([0,T], L^2(0,L))$ and due to higher regularity of $\bar{c}_e^{\pm} \in X$, we even obtain $\partial_x \tilde{c}_e^{\pm} \in C([0,T], L^2(0,L))$. In particular, $\tilde{c}_e^{\pm}$ is continuous with respect to time and space variables since $H^1(\Omega)$ is embedded in $C(\bar{\Omega})$ in one dimension. Moreover, the regularization by means of a cutoff applied to the continuous function $\tilde{c}_e^{\pm} \in X$ also leads to a continuous function, that is, the right-hand side of the ODE is continuous in time. According to the theorem of Picard-Lindelöf, there exists a unique absolutely continuous function c_e^{im}.

We now derive additional estimates for c_e^{im} and its derivatives, which will in turn be needed to investigate the transport equation below. Testing the ODE (12) with c_e^{im} and applying Young's inequality lead to

$$\begin{aligned}\frac{1}{2}\partial_t \|c_e^{im}(t)\|_2^2 &\leq \int_\Omega A^{-1}\left(\tilde{c}_e^{\pm}\right)\left(\tilde{c}_e^{+}\tilde{c}_e^{-} - c_e^{im} + \varepsilon B\left(\tilde{c}_e^{-}\partial_x \tilde{c}_e^{+} + \tilde{c}_e^{+}\partial_x \tilde{c}_e^{-}\right)\right) c_e^{im} \\ &\leq C\left(\|\tilde{c}_e^{+}(t)\|_\infty \|\tilde{c}_e^{-}(t)\|_\infty + \|c_e^{im}(t)\|_2 + \|\tilde{c}_e^{-}(t)\|_\infty \|\partial_x \tilde{c}_e^{+}(t)\|_2 + \|\tilde{c}_e^{+}(t)\|_\infty \|\partial_x \tilde{c}_e^{-}(t)\|_2\right)\|c_e^{im}(t)\|_2 \\ &\leq \frac{3}{2} C\left(\|\tilde{c}_e^{+}(t)\|_\infty^2 \|\tilde{c}_e^{-}(t)\|_\infty^2 + \|\tilde{c}_e^{-}(t)\|_\infty^2 \|\partial_x \tilde{c}_e^{+}(t)\|_2^2 + \|\tilde{c}_e^{+}(t)\|_\infty^2 \|\partial_x \tilde{c}_e^{-}(t)\|_2^2 + \|c_e^{im}(t)\|_2^2\right),\end{aligned} \tag{18}$$

where we used the fact that the denominator $A^{-1}\left(\tilde{c}_e^{\pm}\right)$ is pointwisely bounded by 1 due to the cutoff. The right-hand side is well-defined since the continuous embedding for one spatial dimension described above ensures boundedness. Integration over t and Gronwall's lemma, see Theorem A.4 (with $F_1 = 0$) in the Appendix, implies

$$\begin{aligned}\sup_{t\in(0,T)} \|c_e^{im}(t)\|_2^2 \leq 3C e^{3CT}\Bigg(\|c_{e,0}^{im}\|_2^2 + T\Bigg(&\sup_{t\in(0,T)} \|\tilde{c}_e^{+}\|_\infty^2 \sup_{t\in(0,T)} \|\tilde{c}_e^{-}\|_\infty^2 \\ &+ \sup_{t\in(0,T)} \|\tilde{c}_e^{-}\|_\infty^2 \sup_{t\in(0,T)} \|\partial_x \tilde{c}_e^{+}\|_2^2 + \sup_{t\in(0,T)} \|\tilde{c}_e^{+}\|_\infty^2 \sup_{t\in(0,T)} \|\partial_x \tilde{c}_e^{-}\|_2^2\Bigg)\Bigg),\end{aligned} \tag{19}$$

that is, for sufficiently small times T, terms remain small such that the right-hand side is close to $3C\|c_{e,0}^{im}\|_2^2$. Since the terms $\partial_t c^{im}$ and $\partial_x c^{im}$ enter the right-hand side of the transport Equation (13), we need the following additional estimates: First, we directly consider the ODE (12) to obtain

$$\begin{aligned}\|\partial_t c_e^{im}(t)\|_2 &\leq \left\| A^{-1}\left(\tilde{c}_e^{\pm}\right)\left(\tilde{c}_e^{+}\tilde{c}_e^{-} - c_e^{im} + \varepsilon B\left(\tilde{c}_e^{-}\partial_x \tilde{c}_e^{+} + \tilde{c}_e^{+}\partial_x \tilde{c}_e^{-}\right)\right)\right\|_2 \\ &\lesssim \|\tilde{c}_e^{+}(t)\|_\infty \|\tilde{c}_e^{-}(t)\|_\infty + \|c_e^{im}(t)\|_2 + \|\tilde{c}_e^{-}(t)\|_\infty \|\partial_x \tilde{c}_e^{+}(t)\|_2 + \|\tilde{c}_e^{+}(t)\|_\infty \|\partial_x \tilde{c}_e^{-}(t)\|_2 .\end{aligned} \tag{20}$$

In a similar way as outlined above, see (19), we can extract a prefactor T, after integration with respect to time. Second, we also consider the derivative of the ODE with respect to space and test it with $\partial_x c_e^{im}$. Here, the product rule must be applied, which includes the derivative of the prefactor/denominator $A^{-1}\left(\tilde{c}_e^{\pm}\right)$. However, this contribution can be estimated as outlined below and the L^2-estimate as for the previous considerations for c_e^{im}. The second contribution of the product rule is more crucial and is estimated as follows:

$$\begin{aligned}\frac{1}{2}\partial_t \|\partial_x c_e^{im}(t)\|_2^2 \leq \Bigg(&\frac{\varepsilon}{3D}\|\partial_x \tilde{c}_e^{\pm}\|_2 \|\tilde{c}_e^{+}\tilde{c}_e^{-} - c_e^{im} + \varepsilon B\left(\tilde{c}_e^{-}\partial_x \tilde{c}_e^{+} + \tilde{c}_e^{+}\partial_x \tilde{c}_e^{-}\right)\|_2 + \left(\|\tilde{c}_e^{-}\|_\infty \|\partial_x \tilde{c}_e^{+}\|_2 + \|\tilde{c}_e^{+}\|_\infty \|\partial_x \tilde{c}_e^{-}\|_2\right. \\ &+ \left.\varepsilon|B|\left(2\|\partial_x \tilde{c}_e^{+}\|_4 \|\partial_x \tilde{c}_e^{-}\|_4 + \|\tilde{c}_e^{-}\|_\infty \|\partial_{xx} \tilde{c}_e^{+}\|_2 + \|\tilde{c}_e^{+}\|_\infty \|\partial_{xx} \tilde{c}_e^{-}\|_2\right)\right)\Bigg)\|\partial_x c_e^{im}\|_2 + \|\partial_x c_e^{im}\|_2^2.\end{aligned} \tag{21}$$

The generalized Gronwall's lemma, see Theorem A.4 in the Appendix, implies with $\gamma = 1/2$

$$\sup_{t\in(0,T)} \|\partial_x c_e^{im}(t)\|_2 \leq \left[\|\partial_x c_{e,0}^{im}\|_2 + \int_0^T I(t)\,dt\right]\cdot e^T, \tag{22}$$

where the integrand $I(t)$ is given by

$$\begin{aligned}I(t) = &\frac{\varepsilon}{3D}\|\partial_x \tilde{c}_e^{\pm}\|_2 \|\tilde{c}_e^{+}\tilde{c}_e^{-} - c_e^{im} + \varepsilon B\left(\tilde{c}_e^{-}\partial_x \tilde{c}_e^{+} + \tilde{c}_e^{+}\partial_x \tilde{c}_e^{-}\right)\|_2 + \left(\|\tilde{c}_e^{-}\|_\infty \|\partial_x \tilde{c}_e^{+}\|_2 + \|\tilde{c}_e^{+}\|_\infty \|\partial_x \tilde{c}_e^{-}\|_2\right. \\ &+ \left.\varepsilon|B|\left(2\|\partial_x \tilde{c}_e^{+}\|_4 \|\partial_x \tilde{c}_e^{-}\|_4 + \|\tilde{c}_e^{-}\|_\infty \|\partial_{xx} \tilde{c}_e^{+}\|_2 + \|\tilde{c}_e^{+}\|_\infty \|\partial_{xx} \tilde{c}_e^{-}\|_2\right)\right).\end{aligned} \tag{23}$$

In contrast to the above situations, we cannot simply extract the factor T in (22). However, there holds the embedding

$$\partial_x \tilde{c}_e^{\pm} \in L^2(0,T;H^1(\Omega)) \cap L^\infty(0,T;L^2(\Omega)) \hookrightarrow L^{2/\lambda-\epsilon}(0,T;H^\lambda(\Omega)), \tag{24}$$

where the exponents satisfy $\lambda \in (0,1)$ and $\epsilon > 0$ is sufficiently small; see [Eck]. Choosing $\lambda = 1/2 + \delta$ leads to $H^\lambda(\Omega) \hookrightarrow L^\infty(\Omega)$, and for an embedding into $L^4(\Omega)$, a parameter $\lambda \geq \frac{1}{4}$ is sufficient, that is, $\partial_x \tilde{c}_e^{\pm} \in L^{8-\epsilon}(0,T;L^4(\Omega))$. Finally, a prefactor of the form $T^{\frac{1}{2}}$ can be separated in (22).

Step 3: (**Analyzing the PDE (13) and self-mapping property of** $\mathcal{A}$) In summary, the estimates derived above yield that the right-hand side $-\partial_t c_e^{im} - \varepsilon \partial_x \left(C\left(\tilde{c}^+\tilde{c}^- - c^{im}\right)\right)$ of the transport Equation (13) belongs to $L^\infty(0,T;L^2(\Omega))$. Standard parabolic theory, compare Theorem A.2 in the Appendix, yields the unique existence of a strong solution $c_e^{\pm}$ in X to the linearized transport Equation (13) with

$$\begin{aligned} &\sup_{t\in(0,T)} \|c^{\pm}(t)\|_{H_0^1} + \|c^{\pm}\|_{L^2(H^2)} + \|\partial_t c^{\pm}\|_{L^2(L^2)} \\ &\leq M \left(\|c_{e,0}^{\pm}\|_{H^1} + \|\partial_t c_e^{im} + \varepsilon \partial_x \left(C\left(\tilde{c}^+\tilde{c}^- - c^{im}\right)\right)\|_{L^2(L^2)} \right). \end{aligned} \tag{25}$$

A sufficiently small parameter $T < 1$ even yields $c_e^{\pm} \in X_0$, that is, the fixed point operator $\mathcal{A} : X_0 \to X_0$ introduced in Step 1 is, in fact, a well-defined self-mapping.

Step 4: (**Contraction property**) To finally obtain a fixed point $\bar{c}_e^{\pm} \in X$, it is sufficient to prove the contraction property of the map $\mathcal{A}$. For this purpose, it may be necessary to choose T sufficiently small. Thereby, the proof of Lemma B.1 in Appendix B contains detailed estimates in proving the contraction property.

Step 5: (**Positivity and uniqueness**) Due to the continuity of the obtained fixed points $\bar{c}_e^{\pm}$ and corresponding c_e^{im}, positivity can be ensured at least for a small instant if positive initial data $\bar{c}_{e,0}^{\pm}, c_{e,0}^{im} > 0$ are assumed. Then $\bar{c}_e^{\pm}$ and c_e^{im} represent a solution of the underlying Model 1 without any cutoff. Similar to the proof of the contraction property, uniqueness of the solution can be verified by standard techniques.

Remark 5. If we had applied the standard form of Gronwall's lemma in (21), as in (19), we would not have been able to separate a prefactor T^α anymore because of $\partial_{xx}\tilde{c}_e^{\pm} \in L^2(0,T;L^2(\Omega))$.

Remark 6. The proof also holds for the special situation that no double layer potential is present; that is, the flow is only pressure driven. However, for the case of an evolving geometry, see Model 2, analytical results are not readily possible without significant model simplifications due to numerous nonlinear coupling terms.

4 | NUMERICS

In this section, we present numerical simulations of both models, that is, fixed as well as evolving geometry case, introduced in Section 2. Moreover, we consider, among others, the limit case of a vanishing scaling parameter as a reference, where the related hyperbolic system arises formally from the given models by setting $\varepsilon = 0$, compare Remark 2.

All simulations performed in this paper are implemented in MATLAB [31]. In order to solve the full systems of equations regarded in Section 2, we make use of the integrated function *pdepe*, capable of solving mixed systems of parabolic and elliptic equations in one-dimensional space. After spatial discretization using a finite difference method on uniform meshes, the resulting system of ODEs and algebraic equations is solved using the *ode15s* integrator. This solver employs a variable time-step and variable-order scheme and is specifically tailored to handle stiff and differential-algebraic equations. Due to its robustness, *ode15s* is also used for the treatment of the hyperbolic limit problem $\varepsilon = 0$ (Remark 2) as conducted in Section 4.3 below. To discretize the hyperbolic equation in space, a finite difference scheme with full upwinding is employed. In both cases, simulations are performed on a grid consisting of 1000 nodes.

For our simulations, we use the set of boundary and initial conditions specified in Table 2.

In the hyperbolic limit case, the boundary conditions on the right side of the domain become superfluous due to the flux being strictly pointing in this direction. Furthermore, the set of parameters is chosen according to Table 3.

Throughout our numerical experiments, we consider a third solute species modeling electrically neutral particles. As such, we highlight the effect of the electric field on chemical concentrations. Furthermore, we reconstruct the different shares of dispersion acting on the particles in spatially resolved way, compare Table 1. Note that the cross-coupling term

TABLE 2 Initial and boundary conditions used for numerical simulations.

	Left boundary	Right boundary	Initial condition
c^+	$D = 1$	$N = 0$	1
c^-	$D = 1$	$N = 0$	1
c^{im}/d	-	-	0
p	$D = 1$	$D = 0$	-

Note: D refers to boundary conditions of Dirichlet type, N boundary conditions of Neuman type.

TABLE 3 Choice of parameters for numerical simulations.

L	Φ_R	Φ_L	T	ζ	ϵ	κ	ρ	D
1	0	1	1	0.5	0.01	1	10	0.1

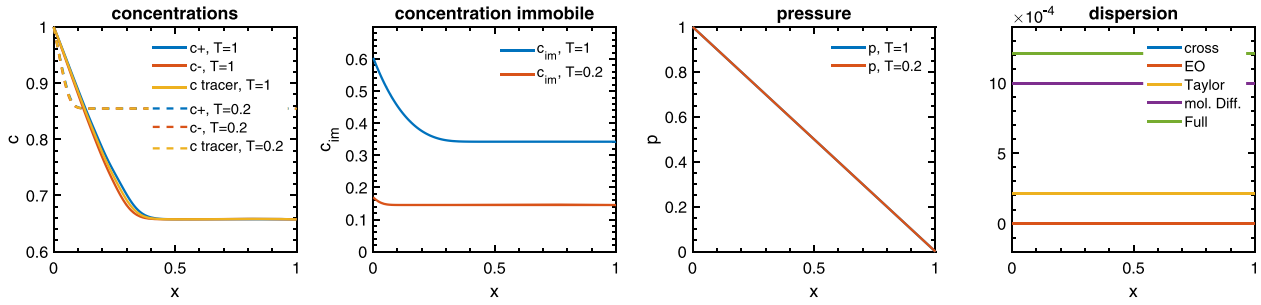

FIGURE 4 Simulation for Model 1, that is, considering a **fixed domain** and **no double layer potential**. Illustrated quantities from left to right: Concentrations of three solute species c^+/c^- plus neutral tracer - concentration of immobile species - pressure within the liquid - dispersion itemized according to the different physical contributions. [Colour figure can be viewed at wileyonlinelibrary.com]

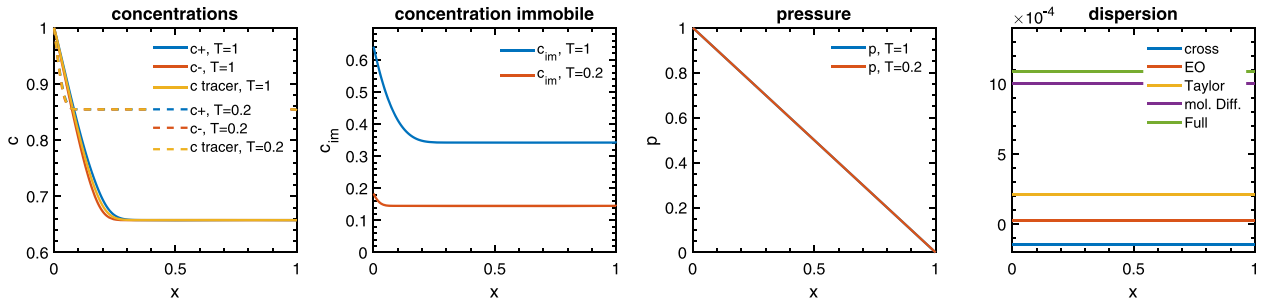

FIGURE 5 Simulation for Model 1, i.e. considering a **fixed domain**, including the effects of a **double layer potential**. Illustrated quantities from left to right: Concentrations of three solute species c^+/c^- plus neutral tracer - concentration of immobile species - pressure within the liquid - dispersion itemized according to the different physical contributions. [Colour figure can be viewed at wileyonlinelibrary.com]

in the dispersive term may have a negative sign, depending on the direction of the electric field. However, Section 3.1 guarantees the positivity of the entire dispersion coefficient.

4.1 | Simulations on fixed geometry

In this section, we perform simulations for Model 1 which exhibits a fixed geometry. First, we consider the simplest case without the formation of double layers, compare Remark 1; see Figure 4.

As expected by the prescribed pressure difference, concentrations are advected from left to right at a velocity of 1/3. Due to precipitation processes, the concentrations of the solute educts reduce over time. Opposed to that, the effects of the electric field on differently charged particles increase over time, steadily separating the three concentration profiles. Apparently, the concentration of the immobile species is highest towards the left boundary where new reactants are supplied. Furthermore, the ratio between the immobile concentration at the left and right boundaries increases over time. Due to the absence of electroosmotic flow, neither electroosmotic nor cross dispersion is present.

This behavior changes when considering the additional formation of a double layer, compare Model 1; see Figure 5. By the interaction of the exterior electric field E and the double layer potential ζ, an additional fluid flow is generated in opposite direction to the negative pressure gradient. As such, the slope of all solute concentrations is higher at the left

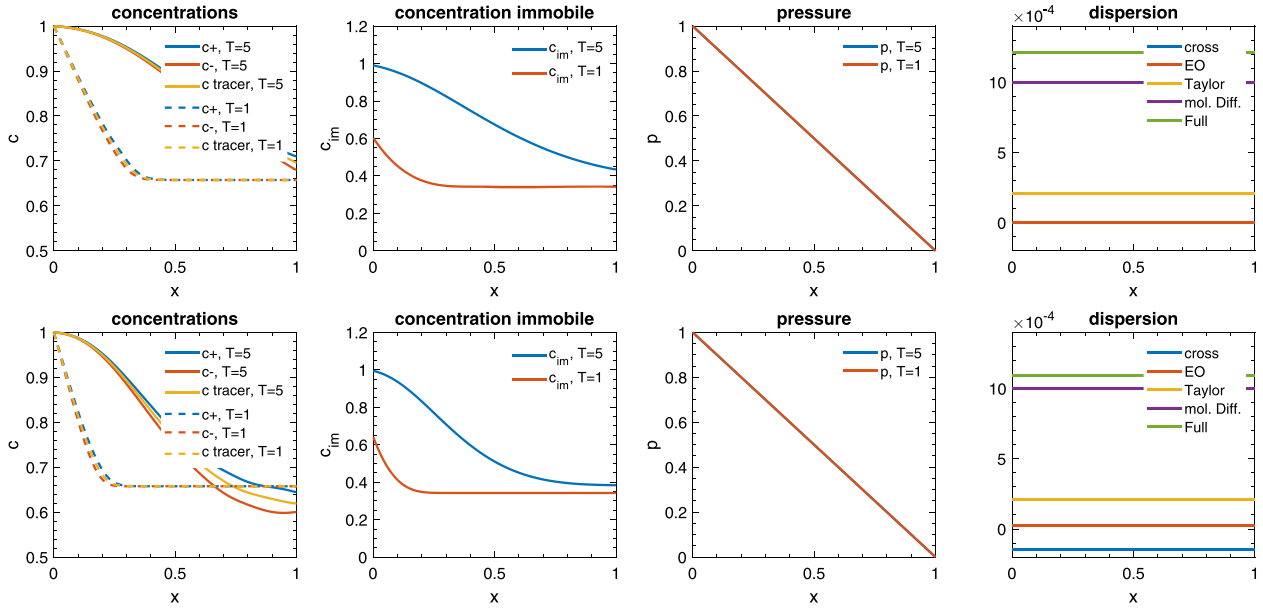

FIGURE 6 Solution behavior for **longer time horizons** $T = 5$. The top illustration refers to Model 1, i.e. fixed geometry, without double layer formation, the bottom one includes double layer formation. [Colour figure can be viewed at wileyonlinelibrary.com]

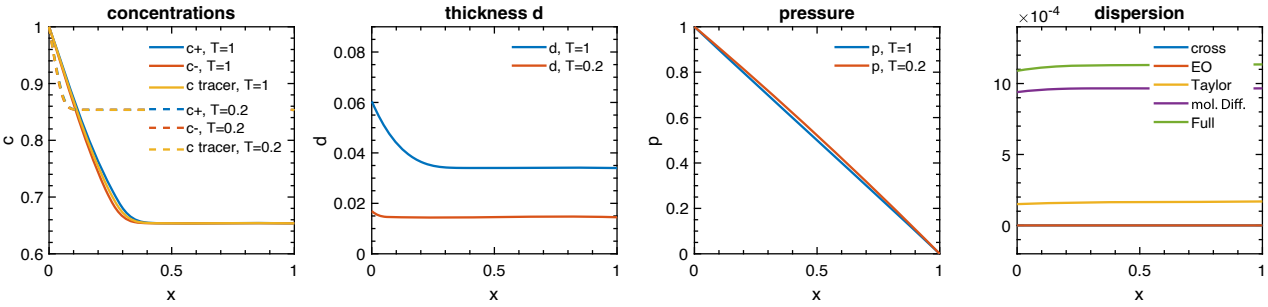

FIGURE 7 Simulation for Model 2, i.e. considering an **evolving domain**, and **no double layer potential**. Illustrated quantities from left to right: Concentrations of three solute species c^+/c^- plus neutral tracer - concentration of immobile species - pressure within the liquid - dispersion itemized according to the different physical contributions. [Colour figure can be viewed at wileyonlinelibrary.com]

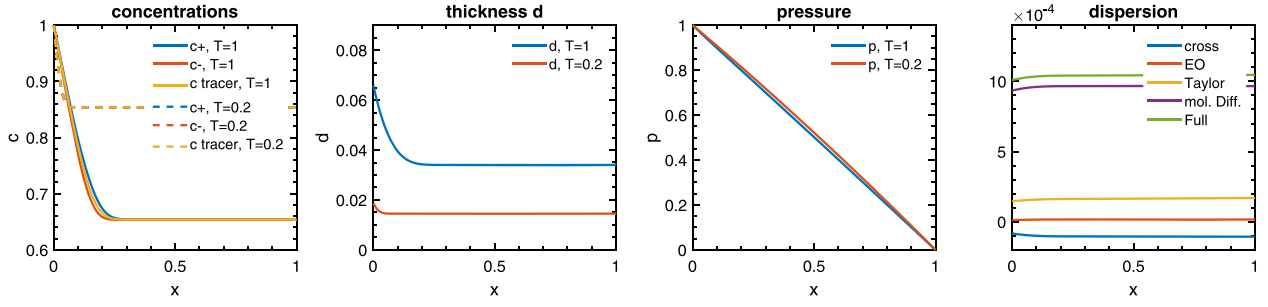

FIGURE 8 Simulation for Model 2, i.e. considering an **evolving domain**, including the effects of a **double layer potential**. Illustrated quantities from left to right: Concentrations of three solute species c^+/c^- plus neutral tracer - concentration of immobile species - pressure within the liquid - dispersion itemized according to the different physical contributions. [Colour figure can be viewed at wileyonlinelibrary.com]

boundary in comparison with the case without double layer formation. Note that the pressure curve is still linear due to the electroosmotic flow field being spatially constant. Moreover, the interaction between pressure and electrically driven flow results in a negative cross dispersion term.

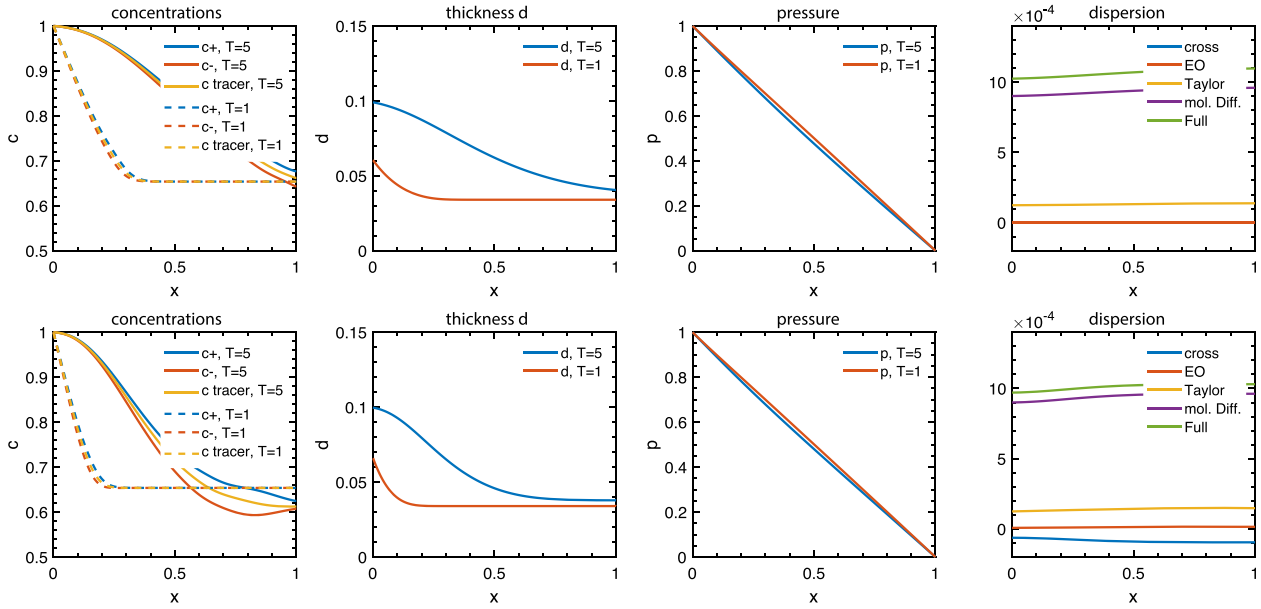

FIGURE 9 Solution behavior for **longer time horizons** $T = 5$. The top illustration refers to Model 2, i.e. the evolving case, without double layer formation, the bottom one includes double layer formation. [Colour figure can be viewed at wileyonlinelibrary.com]

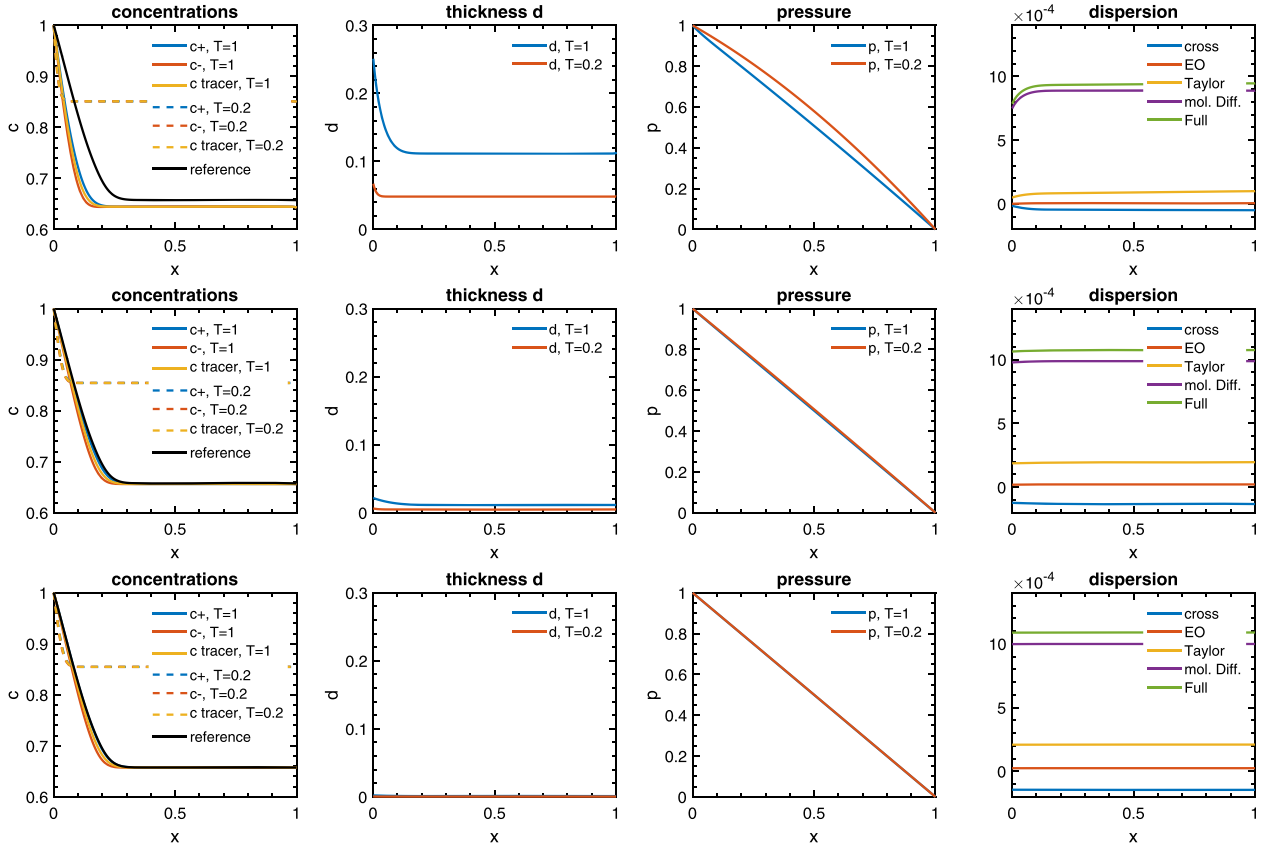

FIGURE 10 Convergence studies for Model 2 with respect to the **density parameter** ρ. Values from top to bottom row: $\rho = 3$, $\rho = 30$, $\rho = 300$. The black reference curve presents the concentration of c^+ at $T = 1$ as obtained from the analogous fixed geometry simulation. [Colour figure can be viewed at wileyonlinelibrary.com]

We note that in both above cases, the solution behavior changes significantly considering larger time horizons. In Figure 6, results are illustrated for $T = 5$. Apparently, dissolution and precipitation reaction have almost equilibrated close to the left boundary, distinctly differing from the steeply descending concentration curves at $T = 1$. Moreover, since

the electric forces acted longer upon the differently charges mobile species, the curves for c^+ and c^- now spread more significantly. This effect appears more pronounced in the presence of a double layer.

4.2 | Simulations on evolving geometry

In this section, we additionally take the effects of an evolving geometry into account which results from the precipitation reaction forming a deposition layer of nonnegligible thickness; see Model 2. Again, we start considering the case without the presence of a double layer potential, compare Remark 1; see Figure 7. The results for the concentration are comparable with the respective case of a fixed domain considered in Section 4.1. However, we note that both pressure-driven fluid velocity and the individual dispersion shares are no longer spatially constant and evolve in time. Due to the aperture of the thin channel constricting at the left boundary, dispersion is reduced in this area.

As before in Section 4.1, the additional presence of a double layer distinctly changes the behavior of system. The related solution is presented in Figure 8 clearly indicating an additional flow field acting on the solute concentration. Note that the reduced thickness of the channel towards the left boundary reduces dispersion, constituting a qualitatively different behavior compared to the previous case of fixed geometry.

The long-term behavior of solution is illustrated for $T = 5$ in Figure 9. Similar to Figure 6, the curves for c^+ and c^- are clearly separated, which again becomes even more evident in the presence of a double layer.

4.3 | Convergence for degenerating parameters

In this section, we investigate the sensitivity of the solutions of Model 2 to the choice of parameters and its consistency with further limit models. More precisely, we consider the following three physical limits cases:

1. $\rho \to \infty$, referring to the limit of large densities of the precipitated layer, i.e. vanishing layer thickness. The result is expected to approximate the scenario on fixed geometries, compare Figure 5.

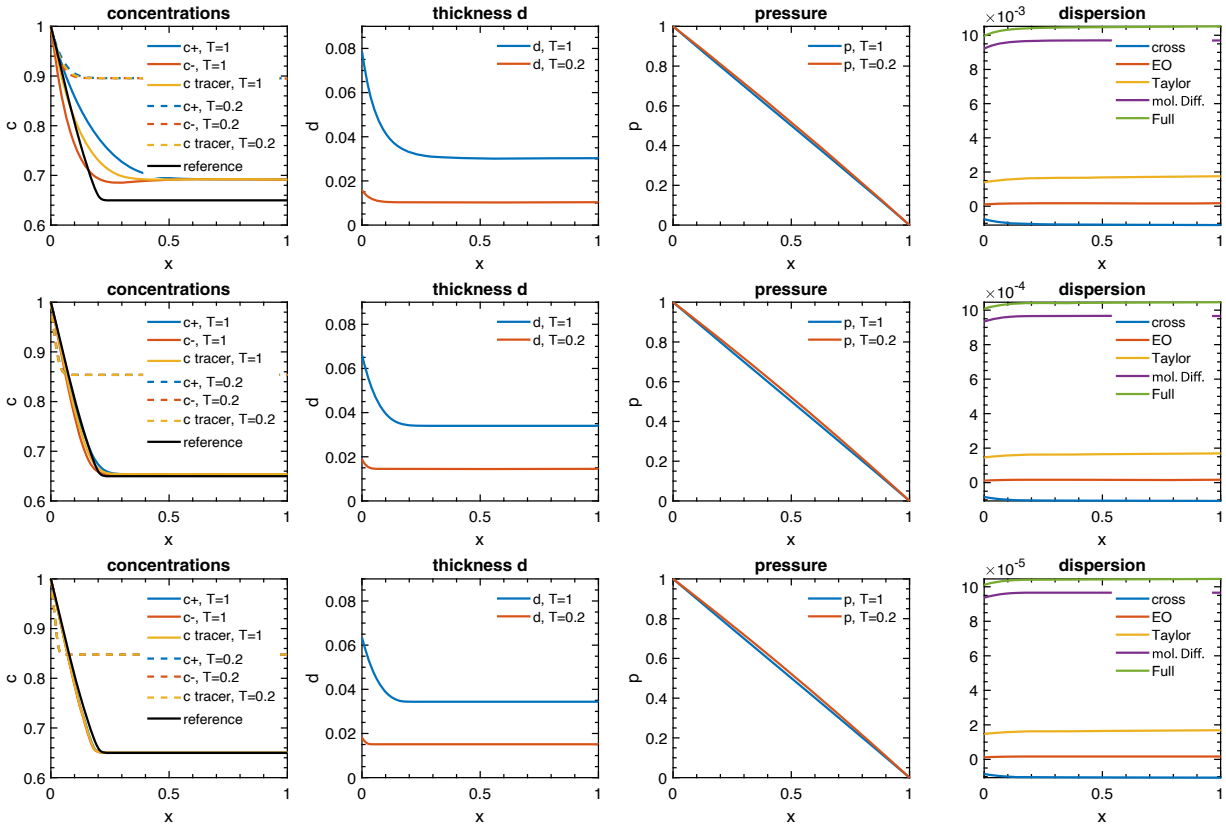

FIGURE 11 Convergence studies for Model 2 with respect to the **scaling parameter** ε. Values from top to bottom row: $\varepsilon = 0.1$, $\varepsilon = 0.01$, $\varepsilon = 0.001$. The reference concentration profile refers to the hyperbolic limit case at $T = 1$. Note the different scaling in the dispersion plots. [Colour figure can be viewed at wileyonlinelibrary.com]

2. $\varepsilon \to 0$, referring to the limit of vanishing channel width. The result is expected to approximate the hyperbolic limit scenario.
3. $D \to 0$, referring to the limit of vanishing molecular diffusion. As such, this setup illustrates the intensifying influences of the other dispersion shares.

4.3.1 | Vanishing precipitation thickness $\rho \to \infty$

In case the density of the precipitating mineral ρ is increased, the thickness of the deposition layer correspondingly decreases. This is investigated in Figure 10. By illustrating the simulation results for densities $\rho = 3$, $\rho = 30$, $\rho = 300$, we indeed conclude a vanishing precipitation layer thickness for $\rho \to \infty$, approximating the case of fixed geometry; see black reference curve in Figure 10 and compare with Figure 5. As expected, the concentration solutions converge to the fixed geometry results. However, severe constrictions of the flow channel as for the case $\rho = 3$, compare Figure 10, top row, result in a reduced influence of dispersion. This effect stems from the fluid displacement caused by the significantly shrinking channel thickness, successively accelerating advective flow. Accordingly, a nontrivial pressure distribution arises.

4.3.2 | Vanishing channel width $\varepsilon \to 0$

As investigated in Kumar et al. [16] for the purely pressure-driven case, we consider the case of vanishing channel width $\varepsilon \to 0$. In Figure 11, the solutions to the model including an evolving geometry are presented exhibiting different values of ε ranging from $\varepsilon = 0.1$, $\varepsilon = 0.01$ to $\varepsilon = 0.001$. As expected, the concentration solutions converge to the ones of the hyperbolic limit problem, which are represented by the black reference curves. Thereby, the hyperbolic model is restricted to the terms of leading order and hence neglects all terms of order ε (and higher), such as the dispersion terms. Apparently, large values of the flow channel's diameter (represented by the parameter ε) increase the overall diffusivity, resulting in a smoothed-out concentration profile. Moreover, the separation among solute species of different electrical charge is promoted due to a stronger coupling of the concentrations to the exterior electric field. As a result, also qualitative changes in the concentration profile become visible for large values of ε. As illustrated for $\varepsilon = 0.1$, compare, Figure 11, top row,

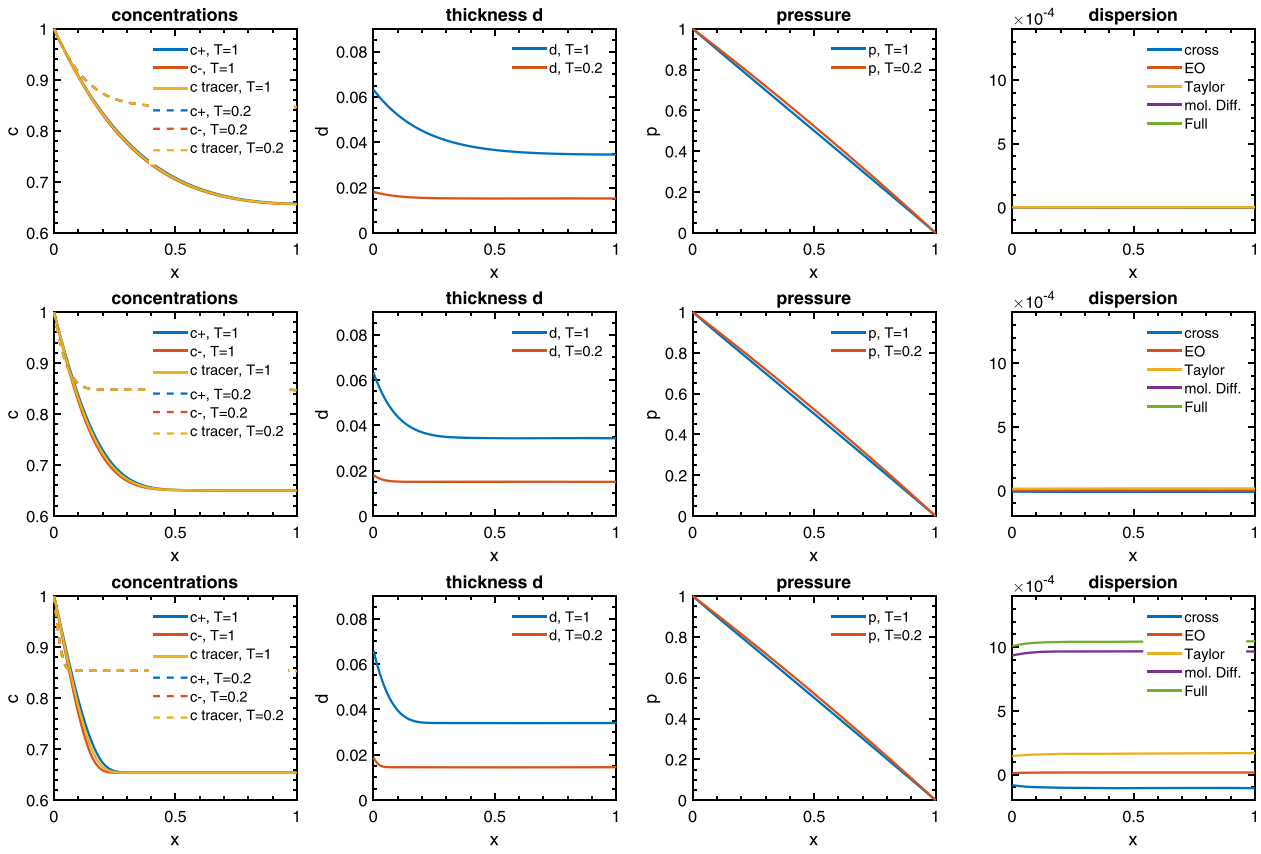

FIGURE 12 Convergence studies for Model 2 with respect to the **molecular diffusion parameter** D. Values from top to bottom row: $D = 10$, $D = 1$, $D = 0.1$. [Colour figure can be viewed at wileyonlinelibrary.com]

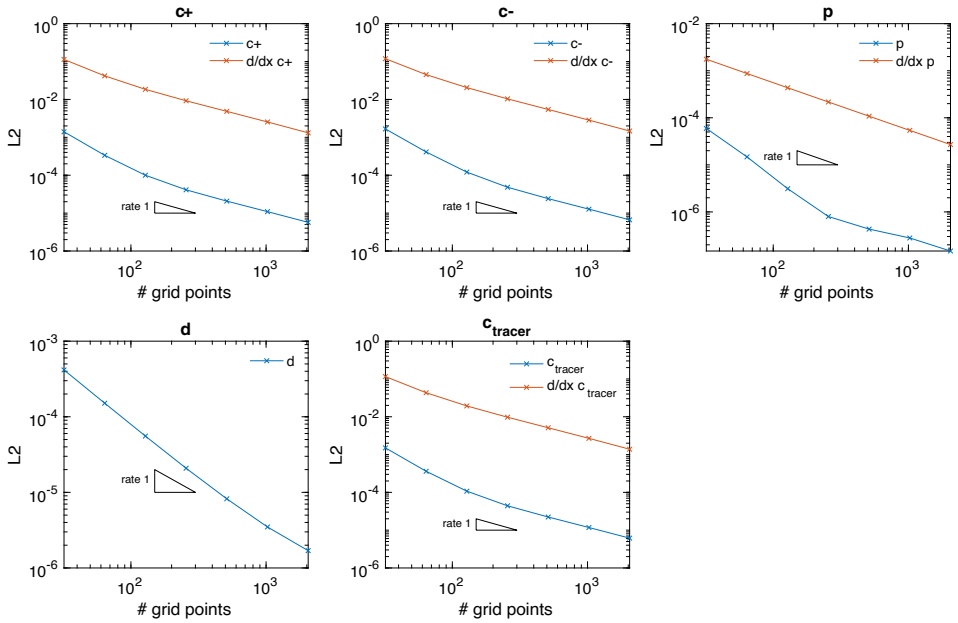

FIGURE 13 Grid convergence for the concentration fields and their gradients, the pressure field, and the layer thickness. The simulations have been performed using $2^i, i \in \{5, \dots, 11\}$ grid points with an L^2 deviation computed as $||\cdot_i - \cdot_{i+1}||_{L^2((0,1))}$ for the quantity $\cdot$ of interest. The slope of the included black triangles corresponds to a linear convergence rate. [Colour figure can be viewed at wileyonlinelibrary.com]

the concentration of negative species c^- exhibits a distinct local minimum at around $x_0 = 0.25$. It appears due to the fact that the product $c^+ \cdot c^-$ is significantly higher in this region than towards the right boundary, increasing the precipitation speed. Since the advection of c^- is, however, inhibited by the external electrical field, c^- is significantly lower than c^+ at x_0.

4.3.3 | Vanishing molecular diffusivity $D \to 0$

Finally, we investigate the behavior associated to vanishing molecular diffusivity $D \to 0$ illustrated in Figure 12. From top to bottom, $D = 10$ is decreased by one order in magnitude per row. Apparently, a lower diffusivity results in a more angular concentration profile. Moreover, high concentrations become more concentrated towards the left boundary, also resulting in a precipitation layer thickness growth focused in this area. Importantly, the decrease in D increases the contribution of Taylor- and cross-diffusion to the overall dispersion. Note that the last share comes with a negative sign.

4.4 | Grid convergence

To validate the numerical scheme, we conduct a convergence study for the fully coupled Model 2 as illustrated in Figure 8 which involves the maximal complexity of all scenarios studied in this paper. Successively increasing the number $2^i, i \in \{5, \dots, 11\}$ of grid points and comparing the i-th and $i+1$-th order, we obtain first-order convergence for the concentrations in H^1 and superlinear convergence for the pressure in L^2 as is evident from Figure 13.

5 | SUMMARY AND CONCLUSION

In this paper, we analytically and numerically investigated novel effective models for reactive flow and transport under dominant advective and electroosmotic flow conditions in a thin, potentially evolving strip as derived in Ray and Schulz [24]. From an analytical perspective, we proved the following:

- the positivity of the emerging rather sophisticated dispersion coefficient, which contains various components (pressure-driven Taylor-dispersion, electroosmotic induced dispersion, and cross-coupling terms); see Table 1 and Section 3.1.
- existence of strong solutions of the underlying partially coupled ODE–PDE system with a fixed point approach for the case of a fixed geometry; see Model 1, Theorem 1, and Section 3.2.

Since the analysis is limited to the fixed geometry setting, further research is needed to address the analysis of Model 2, that is, the case of an evolving pore space; see Remark 6.

Additionally, we conducted numerical simulations. Due to the presence of electric forces, the results illustrated the possibility of separating charged species. This open up ways for improved predictions of breakthrough curves as well as facilitated modeling of mixing and separation processes are possible.

Finally, we numerically studied the convergence behavior of the solutions to the evolving geometry case to the fixed geometry case. To this end, an increased density of the precipitate, that is, decreasing thickness of the precipitated layer was investigated. The relation to the hyperbolic limit model ($\varepsilon = 0$) was investigated. In addition, the contributions of the dispersive terms and the impact on the resulting concentration distribution were underlined by numerical simulations taking into account $D \to 0$. In summary, we conclude that

- the model's solutions to the evolving geometry case converge to the ones of the fixed geometry case for increasing density of the precipitate.
- the model's solutions converge to the hyperbolic limit problem for decreasing scaling parameter ε.
- the contributions of the various dispersive terms significantly influence the steepness of the concentration profiles and the spatial distribution of the precipitate.

These results not only show the consistency with models known from the literature but also allow to judge under which conditions which model choice is most reasonable in terms of accurateness and computational cost. Directions of future research may certainly include model extensions with respect to further drivers of dispersion such as thermal dispersion effects or to more general geometrical settings. Likewise, a sound analytical and numerical treatment of such models is desirable to open up new fields of practical applications.

NOTATION: QUANTITIES AND PARAMETERS INCLUDING THEIR DIMENSIONS IN SI UNITS

$\cdot_0$	zeroth-order quantity
$\cdot_1$	first-order quantity
$\cdot^{(1),(2)}$	horizontal/vertical component of a vector
$\cdot_e$	quantity up to first order
$\cdot_\varepsilon$	scaled quantity
$\cdot_l$	value referring to inflow boundary
$\cdot_r$	value referring to outflow boundary
$\bar{\cdot}$	averaged quantity
$c^{\pm}\ [1/m^2]$	mobile species concentration
$c^{\pm,DL}\ [1/m^2]$	mobile species concentration in double layer
$c^{im}\ [1/m]$	immobile species' concentration
$D\ [m^2/s]$	molecular diffusivity
$E\ [kgm/s^2]$	electric field
$\varepsilon[-]$	scaling parameter
$f\ [kg/(m^2 s)]$	reaction rate
$\Gamma^{\pm}[m]$	upper and lower boundary, potentially evolving
$\Gamma^{in}[m]$	inflow boundary, potentially evolving
$\Gamma^{out}[m]$	outflow boundary, potentially evolving
$\kappa^2\ [1/m^2]$	Debye length
$\nu[-]$	outer unit normal
$\Omega\ [m^2]$	thin strip, potentially evolving
$p\ [kg/(ms^2)]$	pressure
$\phi\ [kgm/s^2]$	electric potential
$\phi^{DL}\ [kgm/s^2]$	double layer potential
$\rho\ [kg/m^2]$	density of boundary layer
$v\ [m/s]$	velocity

AUTHOR CONTRIBUTIONS

Raphael Schulz: Investigation; writing—original draft; formal analysis. **Stephan Gärttner:** Investigation; writing—original draft; visualization; software. **Nadja Ray:** Investigation; writing—original draft; formal analysis.

ACKNOWLEDGEMENTS

This research was initiated by discussions between Nadja Ray and Kundan Kumar, University of Bergen, Norway. The personal exchange was kindly supported by the German Academic Exchange Service (DAAD) in the framework of the German–Norwegian collaborative research support scheme 2016. We gratefully acknowledge financial support from the Deutsche Forschungsgemeinschaft (DFG) within the framework of the DFG Research Unit 2179 "MAD Soil - Microaggregates: Formation and turnover of the structural building blocks of soils" and the DFG Research Training Group 2339 "Interfaces, Complex Structures, and Singular Limits". Open Access funding enabled and organized by Projekt DEAL.

CONFLICT OF INTEREST STATEMENT

This work does not have any conflicts of interest.

ORCID

Raphael Schulz https://orcid.org/0000-0001-9248-6156
Stephan Gärttner https://orcid.org/0000-0002-3488-0929

REFERENCES

1. Y. B. Acar, R. J. Gale, A. N. Alshawabkeh, R. E. Marks, S. Puppala, M. Bricka, and R. Parker, *Electrokinetic remediation: basics and technology status*, J. Hazardous Mater. **40** (1995), no. 2, 117–137. Soil Remediation: Application of Innovative and Standard Technologies.
2. H. Jacob and S. B. Masliyah, *Electrokinetic and colloid transport phenomena*, Wiley, 2006.
3. A. Jamshidi-Zanjani and A. Khodadadi Darban, *A review on enhancement techniques of electrokinetic soil remediation*, Pollution **3** (2017), no. 1, 157–166.
4. X. Xuan, *Recent advances in direct current electrokinetic manipulation of particles for microfluidic applications*, Electrophoresis **40**, no. 18–19, 2484–2513.
5. R. Aris, *On the dispersion of a solute in a fluid flowing through a tube*, Proc. R. Soc. London. Ser. A. Math. Phys. Sci. **235** (1956), no. 1200, 67–77.
6. G. Taylor, *Dispersion of soluble matter in solvent flowing slowly through a tube*, Proc. R. Soc. London. Ser. A. Math. Phys. Sci. **219** (1953), no. 1137, 186–203.
7. J. L. Auriault and P. M. Adler, *Taylor dispersion in porous media: analysis by multiple scale expansions*, Adv. Water Res. **18** (1995), no. 4, 217–226.
8. J. Rubinstein and R. Mauri, *Dispersion and convection in periodic porous media*, SIAM J. Appl. Math. **46** (1986), no. 6, 1018–1023.
9. G. Allaire, R. Brizzi, A. Mikelić, and A. Piatnitski, *Two-scale expansion with drift approach to the taylor dispersion for reactive transport through porous media*, Chem. Eng. Sci. **65** (2010), 2292–2300.
10. C. Choquet and A. Mikelić, *Laplace transform approach to the rigorous upscaling of the infinite adsorption rate reactive flow under dominant Peclet number through a pore*, Appl. Anal. **87** (2008), no. 12, 1373–1395.
11. A. Mikelić, V. Devigne, and C. J. van Duijn, *Rigorous upscaling of the reactive flow through a pore, under dominant Peclet and Damkohler numbers*, SIAM J. Math. Anal. **38** (2006), no. 4, 1262–1287.
12. A. Mikelić and C. Rosier, *Rigorous upscaling of the infinite adsorption rate reactive flow under dominant Peclet number through a pore*, Annali dell' Universit'a di Ferrara **53** (2007), no. 2, 333–359.
13. A. Mikelić and C. J. van Duijn, *Rigorous derivation of a hyperbolic model for Taylor dispersion*, Math. Models Methods Appl. Sci. **21** (2011), no. 05, 1095–1120.
14. C. J. van Duijn, A. Mikelić, I. S. Pop, and C. Rosier, Chapter 1 effective dispersion equations for reactive flows with dominant Péclet and Damkohler numbers, *Advances in chemical engineering mathematics in chemical kinetics and engineering*, D. W. Guy B. Marin and G. S. Yablonsky, (eds.), Advances in Chemical Engineering, vol. **34**, Academic Press, 2008, pp. 1–45.
15. C. Bringedal, I. Berre, S. I. Pop, and F. A. Radu, *Upscaling of nonisothermal reactive porous media flow under dominant Péclet number: the effect of changing porosity*, Multiscale Model. Simul. **14** (2016), no. 1, 502–533.
16. K. Kumar, T. L. van Noorden, and I. S. Pop, *Effective dispersion equations for reactive flows involving free boundaries at the microscale*, Multiscale Model. Simul. **9** (2011), no. 1, 29–58.
17. M. Schmuck and M. Z. Bazant, *Homogenization of the Poisson-Nernst-Planck equations for ion transport in charged porous media*, SIAM J. Appl. Math. **75** (2015), no. 3, 1369–1401.

18. M. Dejam, H. Hassanzadeh, and Z. Chen, *Shear dispersion in combined pressure-driven and electro-osmotic flows in a capillary tube with a porous wallshear dispersion in combined pressure-driven and electro-osmotic flows in a capillary tube with a porous wall*, Am. Inst. Chem. Eng. J. **61** (2015), no. 11, 3981–3995.
19. Z. Kou and M. Dejam, *Dispersion due to combined pressure-driven and electro-osmotic flows in a channel surrounded by a permeable porous medium*, Phys. Fluids **31** (2019), no. 5, 52905.
20. V. Hoshyargar, A. Khorami, S. N. Ashrafizadeh, and A. Sadeghi, *Solute dispersion by electroosmotic flow through soft microchannels*, Sensors Actuators B: Chem. **255** (2018), 3585–3600.
21. R. Talebi, S. N. Ashrafizadeh, and A. Sadeghi, *Hydrodynamic dispersion by electroosmotic flow in soft microchannels: consideration of different properties for electrolyte and polyelectrolyte layer*, Chem. Eng. Sci. **229** (2021), 116058.
22. V. Hoshyargar, M. Talebi, S. N. Ashrafizadeh, and A. Sadeghi, *Hydrodynamic dispersion by electroosmotic flow of viscoelastic fluids within a slit microchannel*, Microfluid Nanofluid **22** (2018), no. 4, 1–15.
23. S. Ayoubi, M. Khatibi, and S. N. Ashrafizadeh, *A variational approach applied to reduce fouling with the electroosmotic flow in porous-wall microchannels*, Microfluid Nanofluid **25** (2021), no. 101, 1–13.
24. N. Ray and R. Schulz, *Derivation of an effective dispersion model for electroosmotic flow involving free boundaries in a thin strip*, J. Eng. Math. **119** (2019), 167–197.
25. T. L. Van Noorden, *Crystal precipitation and dissolution in a thin strip*, Eur. J. Appl. Math. **20** (2009), no. 1, 69–91.
26. T. van Noorden, *Crystal precipitation and dissolution in a porous medium: effective equations and numerical experiments*, Multiscale Model. Simul. **7** (2009), 1220–1236.
27. T. L. van Noorden, I. S. Pop, A. Ebigbo, and R. Helmig, *An upscaled model for biofilm growth in a thin strip*, Water Resour. Res. **46** (2010), no. 6, W06505, DOI 10.1029/2009WR008217.
28. N. Ray, T. Elbinger, and P. Knabner, *Upscaling the flow and transport in an evolving porous medium with general interaction potentials*, SIAM J. Appl.Math. **75** (2015), no. 5, 2170–2192.
29. N. Ray, T. van Noorden, F. Frank, and P. Knabner, *Multiscale modeling of colloid and fluid dynamics in porous media including an evolving microstructure*, Transp. Porous Media **95** (2012), no. 3, 669–696.
30. L. C. Evans, *Partial differential equations*, American Mathematical Society, vol. **19**, Graduate Studies in Mathematics, 1998.
31. MATLAB, *Version 9.10.0.1602886 (r2021a)*, The MathWorks Inc., Natick, Massachusetts, 2021.
32. R. Schulz, N. Ray, F. Frank, H. Mahato, and P. Knabner, *Strong solvability up to clogging of an effective diffusion-precipitation model in an evolving porous medium*, Eur. J. Appl. Math. **28** (2017), no. 2, 179–207.

How to cite this article: R. Schulz, S. Gärttner, and N. Ray, *Investigations of effective dispersion models for electroosmotic flow with rigid and free boundaries in a thin strip*, Math. Meth. Appl. Sci. **47** (2024), 206–228, DOI 10.1002/mma.9651.

APPENDIX A: GENERAL STATEMENTS

Theorem A.1 (Rouché's theorem)**.** *Let f, g be holomorphic functions and $\gamma \subset \mathbb{C}$ be a circle in the comple x plane. If $|f(z)| > |g(z)|$ holds for all $z \in \gamma$, then f and $f + g$ have the same number of zeros inside the circle γ.*

Theorem A.2 (Parabolic regularity, [30, Theorem 5, Chapter 7])**.** *Assume $g \in H_0^1(\Omega)$, $f \in L^2(0,T;L^2(\Omega))$. Suppose $u \in L^2(0,T;H_0^1(\Omega))$ with $\partial_t u \in L^2(0,T;L^2(\Omega))$ is a weak solution of*

$$\begin{aligned} \partial_t u + \mathcal{L}u = \partial_t u - \sum_{i,j=1}^{d} a_{i,j}\frac{\partial^2 u}{\partial x_i \partial x_j} + \sum_{i=1}^{d} a_i \frac{\partial u}{\partial x_i} + au = f(t,x) \quad & \text{in } \Omega_T, \\ u = 0 \quad & \text{on } \partial\Omega_T, \\ u(0,\cdot) = g(x) \quad & \text{in } \Omega. \end{aligned} \tag{A1}$$

Then, for an appropriate constant $M > 0$, the solution $u \in L^2(0,T;H^2(\Omega)) \cap L^\infty(0,T;H_0^1(\Omega))$ and $\partial_t u \in L^2(0,T;L^2(\Omega))$ satisfies the a-priori estimate

$$\sup_{t\in(0,T)} ||u(t)||_{H_0^1(\Omega)} + ||u||_{L^2(0,T;H^2(\Omega)} + ||\partial_t u||_{L^2(0,T;L^2(\Omega))} \leq M\left(||g||_{H_0^1(\Omega)} + ||f||_{L^2(0,T;L^2(\Omega))}\right). \tag{A2}$$

Theorem A.3 (Banach's fixed point theorem, [30, Theorem 1, Chapter 9.2.1]). *Let X_0 be a Banach space. Assume*

$$A : X_0 \to X_0 \tag{A3}$$

is a nonlinear mapping and suppose that

$$\|A[u] - A[\hat{u}]\| \leq \gamma \|u - \hat{u}\|, \qquad u, \hat{u} \in X_0, \tag{A4}$$

where $\gamma < 1$ denotes some appropriate constant. Then A has a unique fixed point.

Theorem A.4 (Generalized Gronwall's lemma [32, Theorem A.1]). *Let F_1 and F_2 be nonnegative and integrable functions on $[0,T]$ and let $\gamma \in (0,1)$ as well as $C > 0$ be constants. Assume that the function $f \in C([0,T])$ satisfies*

$$f(t) \leq C + \int_0^t F_1(s) f(s)^{1-\gamma} ds + \int_0^t F_2(s) f(s) ds \tag{A5}$$

for all $t \in [0,T]$. Then, the inequality

$$f(t) \leq \left[C^\gamma + \gamma \int_0^t F_1(s) ds\right]^{1/\gamma} \exp\left(\int_0^t F_2(s) ds\right) \tag{A6}$$

holds for all $t \in [0,T]$.

APPENDIX B: CONTRACTIVITY

Lemma B.1. *The fixed point operator $\mathcal{A} : X_0 \to X_0$ defined in (16) satisfies the contraction property.*

Proof. Testing the equation satisfied by $c_1^{im} - c_2^{im}$ with $c_1^{im} - c_2^{im}$ leads to

$$\frac{1}{2}\partial_t \left\|c_1^{im} - c_2^{im}\right\|_2^2 \leq \left\|rhs_1^{im} - rhs_2^{im}\right\|_2 \left\|c_1^{im} - c_2^{im}\right\|_2. \tag{B1}$$

Thereby, the term $\left\|rhs_1^{im} - rhs_2^{im}\right\|_{L^2(L^2)}$ can be estimated as follows:

$$\begin{aligned}
\left\|rhs_1^{im} - rhs_2^{im}\right\|_{L^2(L^2)} \leq{}& \left\|A\left(\tilde{c}_1^{\pm}\right)^{-1}\right\|_{L^\infty(L^\infty)} \Big[\left\|\tilde{c}_1^+ - \tilde{c}_2^+\right\|_{L^2(L^2)} \left\|\tilde{c}_1^-\right\|_{L^\infty(L^\infty)} + \left\|\tilde{c}_2^+\right\|_{L^\infty(L^\infty)} \left\|\tilde{c}_1^- - \tilde{c}_2^-\right\|_{L^2(L^2)} \\
&+ \varepsilon|C| \Big\{ \left\|\tilde{c}_1^- - \tilde{c}_2^-\right\|_{L^2(L^\infty)} \left\|\partial_x \tilde{c}_1^+\right\|_{L^\infty(L^2)} + \left\|\tilde{c}_2^-\right\|_{L^\infty(L^\infty)} \left\|\partial_x\left(\tilde{c}_1^+ - \tilde{c}_2^+\right)\right\|_{L^2(L^2)} \\
&+ \left\|\tilde{c}_1^+ - \tilde{c}_2^+\right\|_{L^2(L^\infty)} \left\|\partial_x \tilde{c}_1^-\right\|_{L^\infty(L^2)} + \left\|\tilde{c}_2^+\right\|_{L^\infty(L^\infty)} \left\|\partial_x\left(\tilde{c}_1^- - \tilde{c}_2^-\right)\right\|_{L^2(L^2)} \Big\} \Big] \\
&+ T^{\frac{1}{2}} \left\|A\left(\tilde{c}_1^{\pm}\right)^{-1}\right\|_{L^\infty(L^\infty)} \left\|c_1^{im} - c_2^{im}\right\|_{L^2(L^2)} \\
&+ \left\|A\left(\tilde{c}_1^{\pm}\right)^{-1} - A\left(\tilde{c}_2^{\pm}\right)^{-1}\right\|_{L^2(L^\infty)} \left(\left\|\tilde{c}_2^+ \tilde{c}_2^- - c_2^{im} + \varepsilon B\left(\tilde{c}_2^- \partial_x \tilde{c}_2^+ + \tilde{c}_2^+ \partial_x \tilde{c}_2^-\right)\right\|_{L^\infty(L^2)}\right) \\
=:{}& R_1^{im} + T^{\frac{1}{2}} \left\|A\left(\tilde{c}_1^{\pm}\right)^{-1}\right\|_{L^\infty(L^\infty)} \left\|c_1^{im} - c_2^{im}\right\|_{L^2(L^2)} + R_2^{im},
\end{aligned} \tag{B2}$$

where $\left\|\tilde{c}_2^+\tilde{c}_2^- - c_2^{im} + \varepsilon B\left(\tilde{c}_2^-\partial_x\tilde{c}_2^+ + \tilde{c}_2^+\partial_x\tilde{c}_2^-\right)\right\|_{L^\infty(L^2)}$ can be estimated similarly as in Step 2; see Section 3.2 above. Moreover, there holds

$$\begin{aligned}
&\left\|A\left(\tilde{c}_1^\pm\right)^{-1} - A\left(\tilde{c}_2^\pm\right)^{-1}\right\|_{L^2(L^\infty)} \le \left\|\left(1+\frac{\varepsilon}{2}\frac{\left(\tilde{c}_1^+\right)_+ + \left(\tilde{c}_1^-\right)_+}{D}\right)^{-1} - \left(1+\frac{\varepsilon}{2}\frac{\left(\tilde{c}_2^+\right)_+ + \left(\tilde{c}_2^-\right)_+}{D}\right)^{-1}\right\|_{L^2(L^\infty)} \\
&= \left\|\left(1+\frac{\varepsilon}{2}\frac{\left(\tilde{c}_1^+\right)_+ + \left(\tilde{c}_1^-\right)_+}{D}\right)^{-1}\left(1+\frac{\varepsilon}{2}\frac{\left(\tilde{c}_2^+\right)_+ + \left(\tilde{c}_2^-\right)_+}{D}\right)^{-1}\cdot\frac{\varepsilon}{2D}\left\{\left(\tilde{c}_1^+\right)_+ + \left(\tilde{c}_1^-\right)_+ - \left(\tilde{c}_2^+\right)_+ - \left(\tilde{c}_2^-\right)_+\right\}\right\|_{L^2(L^\infty)} \\
&\le \frac{\varepsilon}{2D}\left(\left\|\left(\tilde{c}_1^+\right)_+ - \left(\tilde{c}_2^+\right)_+\right\|_{L^2(L^\infty)} + \left\|\left(\tilde{c}_1^-\right)_+ - \left(\tilde{c}_2^-\right)_+\right\|_{L^2(L^\infty)}\right).
\end{aligned} \tag{B3}$$

Thus, Gronwall's lemma provides

$$\sup_{t\in(0,T)}\left\|c_1^{im}(t) - c_2^{im}(t)\right\|_2 \le T^{\frac{1}{2}}\left(R_1^{im} + R_2^{im}\right)\cdot e^{T^{\frac{1}{2}}\left\|A\left(\tilde{c}_1^\pm\right)^{-1}\right\|_{L^\infty(L^\infty)}}. \tag{B4}$$

In order to prove the contraction property of the underlying map $\mathcal{A} : X_0 \to X_0$, see Step 1 in Section 3.2; we consider the difference $c_1^\pm - c_2^\pm$ for $c_1^\pm, c_2^\pm \in X$. This difference solves the equation

$$\begin{aligned}
&\partial_t\left(c_1^\pm - c_2^\pm\right) + \partial_x\left(\bar{v}_e\left(c_1^\pm - c_2^\pm\right)\right) - \varepsilon\partial_x\left(\mathbb{D}\partial_x\left(c_1^\pm - c_2^\pm\right)\right) + \varepsilon\partial_x\left(E\left(c_1^\pm - c_2^\pm\right)\right) \\
&= -\partial_t\left(c_1^{im} - c_2^{im}\right) - \varepsilon\partial_x\left(C\left(\tilde{c}_1^+\tilde{c}_1^- - c_1^{im} - \tilde{c}_2^+\tilde{c}_2^- + c_2^{im}\right)\right) =: rhs_{1,2}.
\end{aligned} \tag{B5}$$

Theorem A.2 ensures the inequality

$$\begin{aligned}
\left\|c_1^\pm - c_2^\pm\right\|_X &= \left\|c_1^\pm - c_2^\pm\right\|_{L^\infty(H^1)} + \left\|\nabla^2\left(c_1^\pm - c_2^\pm\right)\right\|_{L^2(L^2)} + \left\|\partial_t\left(c_1^\pm - c_2^\pm\right)\right\|_{L^2(L^2)} \\
&\le M\|rhs_{1,2}\|_{L^2(L^2)};
\end{aligned} \tag{B6}$$

hence, it suffices to estimate the norm with respect to $L^2(0,T;L^2(\Omega))$ of the right-hand side $rhs_{1,2}$. We obtain

$$\|rhs_{1,2}\|_{L^2(L^2)} \le \left(\left\|\partial_t\left(c_1^{im} - c_2^{im}\right)\right\|_{L^2(L^2)} + \varepsilon|C|\left\|\partial_x\left(\tilde{c}_1^+\tilde{c}_1^- - c_1^{im} - \tilde{c}_2^+\tilde{c}_2^- + c_2^{im}\right)\right\|_{L^2(L^2)}\right). \tag{B7}$$

The time derivative of $c_1^{im} - c_2^{im}$ is given by (12), such that $rhs_{1,2}$ can be estimated by

$$\begin{aligned}
&\left\|A\left(\tilde{c}_1^\pm\right)^{-1}\left(\tilde{c}_1^+\tilde{c}_1^- - c_1^{im} + \varepsilon B\left\{\tilde{c}_1^-\partial_x\tilde{c}_1^+ + \tilde{c}_1^+\partial_x\tilde{c}_1^-\right\}\right)\right. \\
&\left. - A\left(\tilde{c}_2^\pm\right)^{-1}\left(\tilde{c}_2^+\tilde{c}_2^- - c_2^{im} + \varepsilon B\left\{\tilde{c}_2^-\partial_x\tilde{c}_2^+ + \tilde{c}_2^+\partial_x\tilde{c}_2^-\right\}\right)\right\|_{L^2(L^2)} \\
&+ \varepsilon|C|\left\{\left\|\partial_x\left(\tilde{c}_1^+ - \tilde{c}_2^+\right)\right\|_{L^\infty(L^2)}\left\|\tilde{c}_1^-\right\|_{L^2(L^\infty)} + \left\|\partial_x\tilde{c}_2^+\right\|_{L^\infty(L^2)}\left\|\tilde{c}_1^- - \tilde{c}_2^-\right\|_{L^2(L^\infty)}\right. \\
&\left. + \left\|\partial_x\left(\tilde{c}_1^- - \tilde{c}_2^-\right)\right\|_{L^\infty(L^2)}\left\|\tilde{c}_1^+\right\|_{L^2(L^\infty)} + \left\|\partial_x\tilde{c}_2^-\right\|_{L^\infty(L^2)}\left\|\tilde{c}_1^+ - \tilde{c}_2^+\right\|_{L^2(L^\infty)} + \left\|\partial_x\left(c_1^{im} - c_2^{im}\right)\right\|_{L^2(L^2)}\right\} \\
&=: R_1 + \varepsilon|C|R_2.
\end{aligned} \tag{B8}$$

For R_1 and $T < 1$, we obtain with (B3) and (B4)

$$\begin{aligned} R_1 \leq & \left\| A\left(\tilde{c}_1^{\pm}\right)^{-1} \right\|_{\infty} T^{\frac{1}{2}} \Big(\|\tilde{c}_1^{+} - \tilde{c}_2^{+}\|_{L^\infty(L^2)} \|\tilde{c}_1^{-}\|_{L^\infty(L^\infty)} + \|\tilde{c}_2^{+}\|_{L^\infty(L^\infty)} \|\tilde{c}_1^{-} - \tilde{c}_2^{-}\|_{L^\infty(L^2)} + \|c_1^{im} - c_2^{im}\|_{L^\infty(L^2)} \\ & + \varepsilon |B| \left\{ \|\tilde{c}_1^{-} - \tilde{c}_2^{-}\|_{L^\infty(L^\infty)} \|\partial_x \tilde{c}_1^{+}\|_{L^\infty(L^2)} + \|\tilde{c}_2^{-}\|_{L^\infty(L^\infty)} \|\partial_x (\tilde{c}_1^{+} - \tilde{c}_2^{+})\|_{L^\infty(L^2)} \right. \\ & \left. + \|\tilde{c}_1^{+} - \tilde{c}_2^{+}\|_{L^\infty(L^\infty)} \|\partial_x \tilde{c}_1^{-}\|_{L^\infty(L^2)} + \|\tilde{c}_2^{+}\|_{L^\infty(L^\infty)} \|\partial_x (\tilde{c}_1^{-} - \tilde{c}_2^{-})\|_{L^\infty(L^2)} \right\} \Big) \\ & + \left\| A\left(\tilde{c}_1^{\pm}\right)^{-1} - A\left(\tilde{c}_2^{\pm}\right)^{-1} \right\|_{L^2(L^\infty)} \left[\|\tilde{c}_2^{+}\tilde{c}_2^{-} - c_2^{im} + \varepsilon B \left\{ \tilde{c}_2^{-} \partial_x \tilde{c}_2^{+} + \tilde{c}_2^{+} \partial_x \tilde{c}_2^{-} \right\} \|_{L^\infty(L^2)} \right] \\ \leq & C_1(T) \left\| \tilde{c}_1^{\pm} - \tilde{c}_2^{\pm} \right\|_X . \end{aligned} \tag{B9}$$

The term in the square brackets is bounded and can be estimated in the same way as (20).

With an inequality similar to (22), we can estimate the remaining term R_2. More precisely, we also obtain a constant $C_2(T)$ depending on $T < 1$, such that

$$R_2 \leq C_2(T) \left\| \tilde{c}_1^{\pm} - \tilde{c}_2^{\pm} \right\|_X . \tag{B10}$$

Finally, for sufficiently small T, we obtain $C_0(T) := M(C_1(T) + \varepsilon |C| C_2(T)) < 1$, and hence, the contraction property of the map $\mathcal{A}$, that is,

$$\left\| c_1^{\pm} - c_2^{\pm} \right\|_X \leq C_0(T) \left\| \tilde{c}_1^{\pm} - \tilde{c}_2^{\pm} \right\|_X . \tag{B11}$$

□